Fluctuation-driven topological Hall effect in room-temperature itinerant helimagnet Fe_3Ga_4

Priya R. Baral,[1,2,3,*] Victor Ukleev,[1,4] Ivica Živković,[2] Youngro Lee,[2] Fabio Orlandi,[5] Pascal Manuel,[5] Yurii Skourski,[6] Lukas Keller,[1] Anne Stunault,[7] J. Alberto Rodríguez-Velamazán,[7] Robert Cubitt,[7] Arnaud Magrez,[2] Jonathan S. White,[1] Igor I. Mazin,[8,9] and Oksana Zaharko[1,†]

[1]*Laboratory for Neutron Scattering and Imaging (LNS), PSI Center for Neutron and Muon Sciences, 5232 Villigen PSI, Switzerland*

[2]*Institute of Physics, École Polytechnique Fédérale de Lausanne (EPFL), CH-1015 Lausanne, Switzerland*

[3]*Department of Applied Physics and Quantum-Phase Electronics Center, The University of Tokyo, Bunkyo-ku, Tokyo 113-8656, Japan*

[4]*Helmholtz-Zentrum Berlin für Materialien und Energie, D-14109 Berlin, Germany*

[5]*ISIS Facility, STFC Rutherford Appleton Laboratory, Harwell Science and Innovation Campus, Oxfordshire OX11 0QX, United Kingdom*

[6]*Dresden High Magnetic Field Laboratory (HLD-EMFL), Helmholtz-Zentrum Dresden-Rossendorf, 01328 Dresden, Germany*

[7]*Institut Laue–Langevin, 71 avenue des Martyrs, CS 20156, Grenoble, 38042 Cedex 9, France*

[8]*Department of Physics and Astronomy, George Mason University, Fairfax, VA 22030*

[9]*Center for Quantum Science and Engineering, George Mason University, Fairfax, VA 22030*

[*] baralp@g.ecc.u-tokyo.ac.jp

[†] oksana.zaharko@psi.ch

ABSTRACT

The topological Hall effect (THE) is a hallmark of a non-trivial geometric spin arrangement in a magnetic metal, originating from a finite scalar spin chirality (SSC). The associated Berry phase is often a consequence of non-coplanar magnetic structures identified by multiple k-vectors. For single-k magnetic structures however with zero SSC, the emergence of a finite topological Hall signal presents a conceptual challenge. Here, we report that a fluctuation-driven mechanism involving chiral magnons is responsible for the observed THE in a low-symmetry compound, monoclinic Fe_3Ga_4. Through neutron scattering experiments, we discovered several nontrivial magnetic phases in this system. In our focus is the helical spiral phase at room temperature, which transforms into a transverse conical state in applied magnetic field, supporting a significant THE signal up to and above room temperature. Our work offers a fresh perspective in the search for novel materials with intertwined topological magnetic and transport properties.

INTRODUCTION

The study of quantum materials with non-trivial topological properties has gained increasing popularity in condensed matter physics due to their potential applications in ultra-low-power electronic devices [1–3]. The topological nature of these materials is determined by the emergent magnetic field arising from the unique geometric properties of the electronic band (spin) structure in reciprocal (real) space, which have the potential to support a locally enhanced Berry curvature. The anomalous Hall conductivity is a direct experimental manifestation of the topological contributions from these bands, appearing as an additional component to the normal Hall signal [4, 5]. Moreover, the overall Hall signal may exhibit a third component, known as the topological (or geometrical) Hall effect (THE), which arises from noncoplanar spin arrangements in real space. The latter is quantified by the so-called static scalar spin chirality (SSC), defined as $\chi_{ijk} = \mathbf{S}_i \cdot (\mathbf{S}_j \times \mathbf{S}_k)$ in the discrete (localized-spins) limit with $\mathbf{S}_{i,j,k}$ being neighboring spins, forming a triangle electrons can hop around [6]. Equivalently, in the continuous limit of magnetisation $\mathbf{m}$ relatively slowly varying in space, the same quantity can be defined in terms of a vectors variable, called "emergent magnetic field", as $\mathcal{B}_\alpha = 1/2 \sum_{\beta\gamma} e_{\alpha\beta\gamma} \mathbf{m} \cdot (\partial_\beta \mathbf{m} \times \partial_\gamma \mathbf{m})$, where α, β and γ are Cartesian coordinates in real space. This emergent field deflects conduction electrons and produces a finite THE, among other emergent phenomena [3, 7–9].

Not all noncoplanar structures generate a finite scalar spin chirality. For instance, a conical spiral (see Fig. 1a), described by the equation $d\mathbf{m}/dz = \mathbf{\Omega} \times \mathbf{m} + \mathbf{m}'$, where z is the direction of the spiral propagation, and $\mathbf{\Omega}$ and $\mathbf{m}'$ are arbitrary vectors, obviously has zero emergent field, even in the noncoplanar case of $\mathbf{m}' \cdot \mathbf{\Omega} \neq 0$, because for a nonzero $\mathcal{B}$ one needs to have magnetisation varying along two independent directions. Similarly, a combination of two helical spirals can also not generate $\mathcal{B} \neq 0$. Indeed, one can show that in this case $\mathcal{B} = 1/2\ m^2 \mathbf{m} \cdot (\mathbf{\Omega_1} \times \mathbf{\Omega_2})$, which averages to zero.

However, it was realized in recent years that multiple spirals can generate THE, if they are properly combined. This includes three independent spirals (and each of them can be flat) [10–13], or two spirals combined with a net uniform magnetisation (as indicated by the equation above) [14–16], as well as other noncoplanar arrangements that cannot be described as combinations of spirals [17, 18].

Interestingly, significant topological Hall signals have been recently observed in a topologically trivial magnetic phase of kagome-layered YMn_6Sn_6, known as the transverse conical spiral (TCS) state, which formally carries zero scalar chirality and emergent field [19]. As schematically shown in Fig. 1a, the TCS state is obtained after a spin-flop while applying an in-plane magnetic field to the

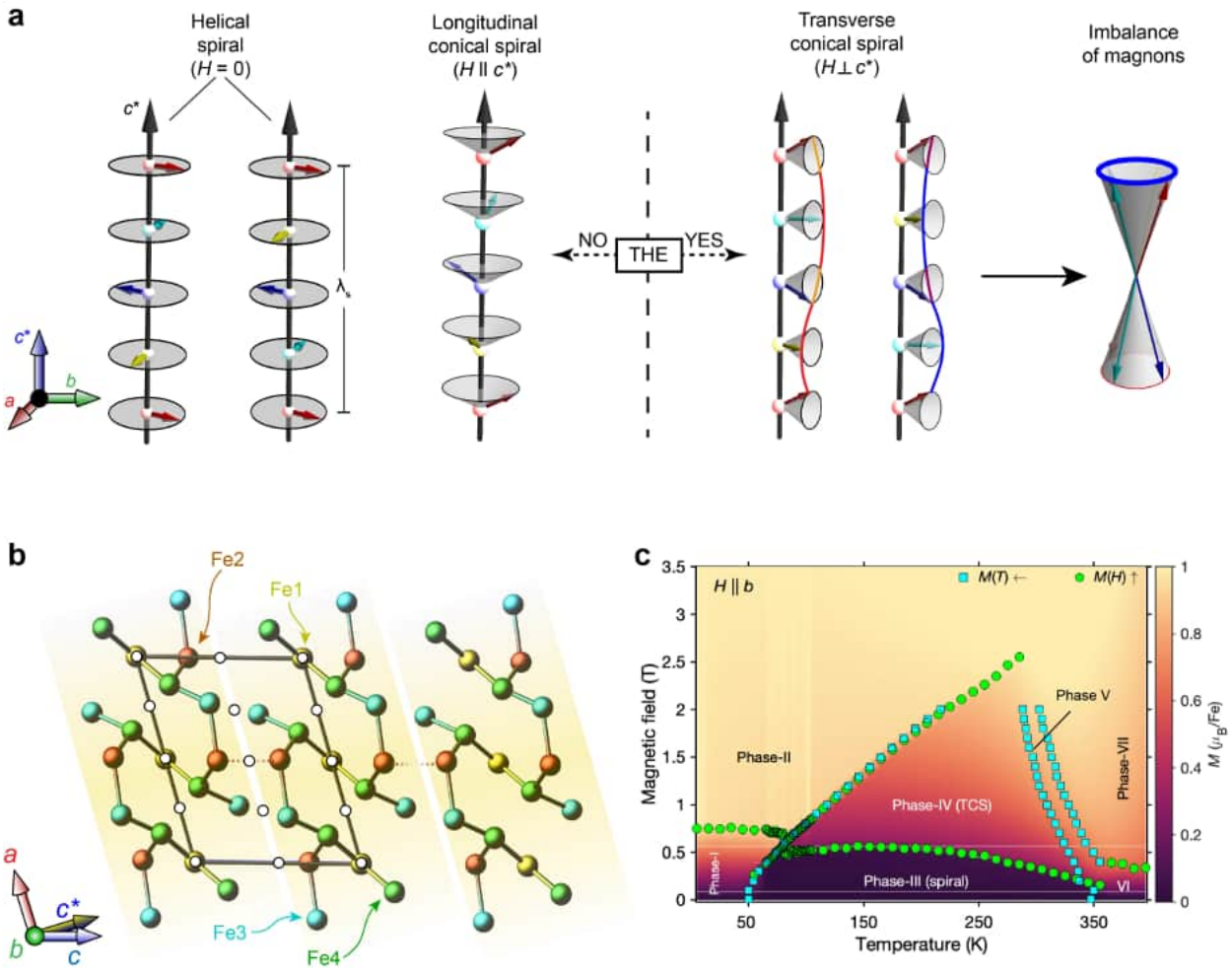

FIG. 1. **Magnetic field induced dynamical scalar spin chirality in Fe_3Ga_4 .a,** Schematics of the two counter-rotating spirals propagating along c^* and $-c^*$, respectively. A longitudinal (transverse) conical spiral state is formed when magnetic field is applied along (orthogonal to) the direction of spiral propagation. Preferential excitation of magnons with a particular handedness generates a dynamic scalar spin chirality. The topological Hall effect could exist in the cases shown to the right and could not in the cases to the left. **b**, Unit cell of Fe_3Ga_4 projected onto the ac-plane showing four inequivalent Fe_{1-4}-sites (filled colored circles) and the inversion centers (empty black circles). The overall structure can be conceived as Fe-slabs stacked along the c-axis, schematically shown by yellow shaded regions. Two different types of the Fe-Fe paths (shorter than 2.95 Å) are drawn: the intra-slab couplings are shown by solid lines, while the dashed lines represent the inter-slab couplings along the c-axis. **c,** Magnetic phase diagram constructed from temperature and field dependent magnetisation measurements. The color map corresponds to the magnetisation evolution in various phases.

helical spiral and can be visualized as a cycloid propagating orthogonally to the applied magnetic field, together with a uniform magnetisation along the field. The appearance of a THE in YMn_6Sn_6

is attributed to a *dynamical* effect, where directional breaking of time-reversal symmetry leads to an unbalanced population of chiral magnons with a given handedness, i.e. a nematic spin chirality. The resulting susceptibility generates the necessary SSC to promote the THE signal at elevated temperatures, and the THE amplitude is roughly proportional to the temperature. Experimental realisations of fluctuation-driven THE are currently scarce and largely restricted to the family of hexagonal $R\mathrm{Mn_6Sn_6}$ compounds [19–21], though the theory is generic and is not limited to any symmetry of the lattice.

In this connection, it would be intriguing to discover other non-chiral materials that nevertheless exhibit topological Hall effect arising due to the fluctuation-driven mechanism. To this end, we turn our attention to the itinerant magnet $\mathrm{Fe_3Ga_4}$. We construct a more detailed magnetic phase diagram with additional phases compared to the ones currently found in literature by combining high-resolution magnetometry and electrical transport data [22, 23]. Our neutron diffraction results, combined with spherical neutron polarimetry (SNP), provide strong support for the helical spin arrangement at elevated temperatures with moments rotating in the ab-plane, which flops into a TCS state in magnetic fields applied along the a- or b-axis. We propose that the observed THE results from an unbalanced excitation of chiral magnons in an applied magnetic field, suggesting a dynamic origin of the SSC. This mechanism is conceptually similar to that in $\mathrm{YMn_6Sn_6}$, but occurs in a completely different magnetic material. The topological Hall signal, which is proportional to the emergent magnetic field generated by this SSC, varies linearly with temperature at a fixed magnetic field. This observation strengthens our claims about its dynamic origin. The results obtained for the TCS phase as well as for the zero field helical spiral phase are discussed in conjunction with other regimes of the thoroughly explored phase diagram. The magnitude of the topological Hall signal is comparable to that measured in topologically non-trivial skyrmion hosts. Our findings demonstrate an alternative route for generating a geometrical Hall response in itinerant spiral magnets at elevated temperatures.

RESULTS

Crystal structure and complex magnetic phase diagram of $\mathrm{Fe_3Ga_4}$

Our target material crystallises in a centrosymmetric structure shown in Fig. 1b with the monoclinic unit cell ($C2/m$, a = 10.0966(5) Å, b = 7.6650(4) Å, c = 7.8655(4) Å, and β = 106.25(4)° at T = 300 K [24]). Results from detailed structural characterisation using single crystal X-ray diffraction can be found in supplementary materials section I. The complicated network of four inequivalent Fe-sites can be separated into Fe-slabs stacked along the c-axis. Within each slab the

nearest iron distance does not exceed 2.95 Å and majority of the Fe-bonds contain no inversion center at the middle, allowing for local Dzyaloshinskii–Moriya interaction (DMI). The Fe slabs have not only geometrical, but also electronic relevance for magnetic properties discussed below, since the DFT spin spiral calculations [25] point to the energy minimum for magnetic spirals with propagation vectors along the $\mathbf{Q} = (0, 0, q_z)$ reciprocal lattice vector.

The complex magnetic phase diagram in Fig. 1c contains numerous phases which we identify by magnetisation and ac susceptibility measurements. As shown later in this article, various scattering techniques together with transport measurements have been used to understand the macroscopic features of the identified phases. Magnetisation data presented in Fig. 2a indicates magnetic ordering of Fe_3Ga_4 at temperature T_4 around 720 K. On cooling three successive magnetic transitions could be distinguished, at $T_3 \simeq 420$ K, $T_2 \simeq 370$ K and $T_1 \simeq 53$ K signaling the onset of Phases VI, III and I, respectively. The existence of the previously unreported Phase V is evident from the additional magnetometry data presented in supplementary materials Fig. S2b. As discussed later in the article, we also observe strong signatures at the boundaries of Phase V in the electrical transport measurements.

Non-coplanar magnetic order at zero field in Phase III

A THE signal was previously detected in applied magnetic field within the temperature range 68 K $<T<$ 360 K [22], which corresponds to Phase IV in our magnetic phase diagram shown in Fig. 1c. Thus, our discussion starts with the nature of magnetic order arising in the zero field state within the same temperature range, that is Phase III. As shown in Fig. 2a, in presence of a small magnetic field, the occurrence of this phase is signaled by a strong gradual reduction in the magnetic moment at the high-T side, T_2, and by an order of magnitude sharp increase in the net magnetisation at the low-T side, T_1. To characterise magnetic anisotropy in Phase III we measure the change of magnetisation within the ac- and a^*b-planes (Figure 2b). Apparently, magnetisation follows the order $m_c \gg m_a \geq m_b$ suggesting almost equal moment distribution in the ab-plane. A possible interpretation consistent with this scenario could be a spiral propagating along c^* direction, whose local moments are confined within the ab-plane.

A previous neutron diffraction study showed that phase III is incommensurate (ICM), with the propagation vector $\mathbf{k} = (0\ 0\ \gamma)$, where γ is temperature dependent and varies between $\sim$0.24 and $\sim$0.29 r.l.u.[26]. Two contradicting models for the ICM magnetic order are proposed: an amplitude modulated spin density state (ASDW) and a helical state, both propagating along c^*. While in the ASDW model magnetic moments are confined within the ac-plane with only the Fe_4

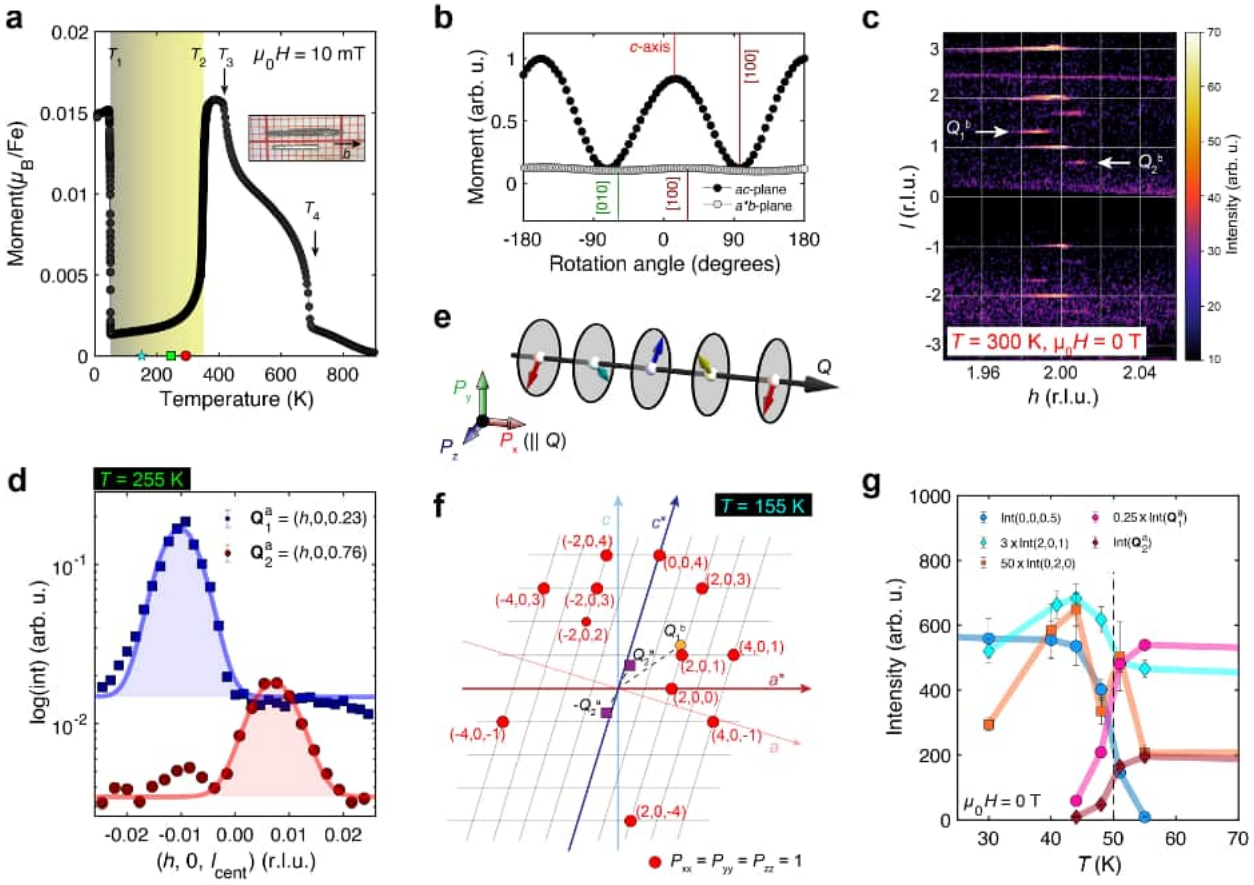

FIG. 2. **Non-coplanar helimagnetism in Fe_3Ga_4 at room temperature.** **a,** Temperature dependence of magnetisation between 5 K and 900 K in 10 mT magnetic field applied along the b-axis with four transitions labelled $T_1 - T_4$. Helimagnetism observed in Phase III is schematically shown as a shaded region between T_1 and T_2. Inset shows typical Fe_3Ga_4 single crystals used in this study. Cyan, green and red symbols represent the corresponding temperatures for spherical neutron polarimetry (SNP) on D3, single crystal diffraction on DMC and WISH instruments, respectively. **b,** The measured $M(\psi)$ curves for a rotating single crystal under a constant magnetic field of 100 mT applied normal to the plane of measurement at 155 K. **c,** Orthogonal projection of the monoclinic (h 0 l) reciprocal lattice plane at $T = 300$ K obtained from data collected on the WISH diffractometer. The small deviations from the (h,0,l) line ($h = 2$) for the magnetic satellites indexed with $\mathbf{Q}_1^{\mathrm{b}}$ and $\mathbf{Q}_2^{\mathrm{b}}$ are apparent. **d,** Order of magnitude difference in the intensity of $\mathbf{Q}_1^{\mathrm{a}}$ and $\mathbf{Q}_2^{\mathrm{a}}$ obtained at 255 K. **e,** Local coordinate axes in the SNP experiment, where P_x component of the incoming neutron beam is aligned along the **Q**-direction of each reflection. **f,** All reflections probed with the SNP experiment at 155 K. **g,** Temperature dependence of intensity of several Bragg peaks tracked in the vicinity of T_1 while warming.

moments possessing a small b-component [26], the magnetic moments rotate in the ab-plane in the helical model [25, 27].

In order to clarify the nature of magnetic order in Phase III we employ a combination of single crystal neutron diffraction (SND) and SNP experiments (see Methods for further details). A snapshot of the reciprocal space map obtained with high-resolution on the time-of-flight diffractometer WISH at ISIS is shown in Fig. 2c. Besides the ICM c* component reported earlier by Wu *et al.* [26], we also detect a small component along h (Fig. 2c & d). Thus the ICM reflections should be properly indexed as ($h+\alpha$, 0, $l+\gamma$). This does not lower the magnetic symmetry however, since ($h+\alpha$, 0, $l+\gamma$) and (0, 0, $l+\gamma$) belong to the same plane of symmetry in the first Brillouin zone. Both α and γ change with temperature and field. At T = 255 K for a low$-\mathbf{Q}$ reflection $\mathbf{Q}_2^{\rm a}$, α and γ are determined to be 0.007 and -0.240, respectively, see Fig. 2d. The other low$-\mathbf{Q}$ satellite $\mathbf{Q}_1^{\rm a}$ inside the first Brillouin zone can be indexed with -α and -γ within the precision of the measurement, which suggest presence of two chiral domains, this is elaborated further below.

In the next step, the directional information about the magnetisation distribution in Phase III is deduced from our SNP experiment. The experimental setup is schematically shown in Fig. 2e, where the direction of the incident neutron polarisation is fixed relative to $\mathbf{Q}$. The measured polarisation matrices P_{ij} (i- the row-index of incoming polarisation, j- the column index for outgoing polarisation) are presented in supplementary materials. The analysis of three components of the scattered beam makes SNP a powerful tool to study non-coplanar magnetic orders.

Several reflections were measured in the ($h0l$) scattering plane, see the full map in Fig. 2f. For the reflection $\mathbf{Q}_2^{\rm a}$=(0.007, 0, 0.759) we obtain finite chiral matrix elements: P_{yx} = -0.43(5) and P_{zx} = -0.48(5). This establishes a helical nature of the magnetic order. P_{xx} equals -1.04(3), implying a purely magnetic origin, while the remaining elements are zero. The polarisation matrix for the $\mathbf{Q}_1^{\rm b}$=(1.99, 0, 1.28) reflection also has finite chiral elements, but of the positive sign, opposite to $\mathbf{Q}_2^{\rm a}$. From the finite and opposite sign P_{yy}, P_{zz} elements for the $\mathbf{Q}_1^{\rm b}$ reflection we extract that the magnetic component along the local z- (crystal b-) axis is larger than the magnetic component along the y- (approximately (101)- crystal) axis. In summary, Phase III is unambiguously determined to be helical and chiral domains are unequally populated allowing for a net spin chirality. In addition, the magnetic arrangement might be three-dimensional. Regrettably, a reliable collection of intensity data-set was not possible due to an insufficient quality of crystals at this low temperature, therefore the microscopic model of Phase III cannot be developed further. Still, in accordance with the magnetic anisotropy results, the moments should be located predominantly in the ab-plane.

As the temperature decreases, around T_1, we observe a narrow coexisting region between Phase III and Phase I (see Fig.2g). In Phase I, in addition to the ferromagnetic component ($\mathbf{k}$ = 0)

reported in Refs. [22, 26], we detect a $\mathbf{k}$ = (0 0 1/2) propagation vector and associated antiferromagnetic commensurate order, which was previously overlooked. Phase I and its transformation into Phase II in magnetic field are discussed in details in Supplementary material.

Magnetic field-induced effects in Fe_3Ga_4

Isothermal magnetisation and susceptibility measured at T = 155 K (Figs. 3a, b) disclose two transitions induced by magnetic field applied along the b-axis: at H_{c1} = 0.55 T and H_{c2} = 1.4 T. The step-like increase in magnetisation are clear signatures of the successive transitions from Phase III to Phase IV and then to Phase II. Around H_{c2}, there is a clear hysteresis revealing the first-order nature of the transition between these phases. As shown in Fig. 3a, at T = 155 K there is no hysteresis around $\mu_0 H = 0$ T. This is corroborated by our SNP results, since full polarisation matrices for the measured $\mathbf{k}$ = 0 reflections suggest only nuclear, no magnetic contributions (see Supplementary material). These results indicate the absence of any ferromagnetic component in Phase III of Fe_3Ga_4 .

Next we follow neutron diffraction signatures of the magnetic field induced phases emerging out of Phase III. As shown in Fig. 3c, intensity of the $\mathbf{Q}_2^a$ reflection is approximately halved in Phase IV compared to the zero field value. The reduction is abrupt at H_{c1} and H_{c2} and it correlates with the derivative of magnetisation $\Delta M/\Delta H$, while within Phases III and IV the intensity is constant. This behaviour suggests the moment reorientation from the ab- to ac- plane, hence the transformation of the incommensurate modulation from a helix to a cycloid. The magnetic field-induced phase changes also have subtle manifestation in the longitudinal resistivity data measured throughout Phase IV, as shown in Fig 3c & d, indicating a discontinuous transformation between Phases IV and II. A weak (strong) change observed in ρ_{xx} at H_{c1} (H_{c2}) indicates a rather weak (strong) charge-spin coupling at the corresponding transitions.

The positional shift of ICM reflections is also strong but continuous with field (Fig. 3e & f). For the $\mathbf{Q}_1^a$ reflection at T = 255 K the l-value increases from 0.2263(5) at $\mu_0 H$ = 0 T to 0.3298(3) at $\mu_0 H$ = 2.3 T resulting in $\Delta l/\bar{l}$= 18.6%. For the $\mathbf{Q}_2^a$ reflection $\Delta(1-l)/\overline{(1-l)}$=17.6%, and the h-values change by a similar amount (Fig. 3e). Fig. 3g and h present the field evolution of the q_z-component in Phase IV for the $\mathbf{Q}_2^a$ and $\mathbf{Q}_1^a$ reflections, respectively. The field dependence is linear and the $l(H)$ slope is positive revealing the tendency towards a commensurate structure with q_z=1/3, as schematically depicted in Fig. S4. Further field dependence of $\mathbf{Q}_1^a$ reflection is depicted in supplementary material section V. However, as shown in the supplementary material, the q_z=1/2 magnetic order develops at low temperatures and elevated magnetic fields, suggesting

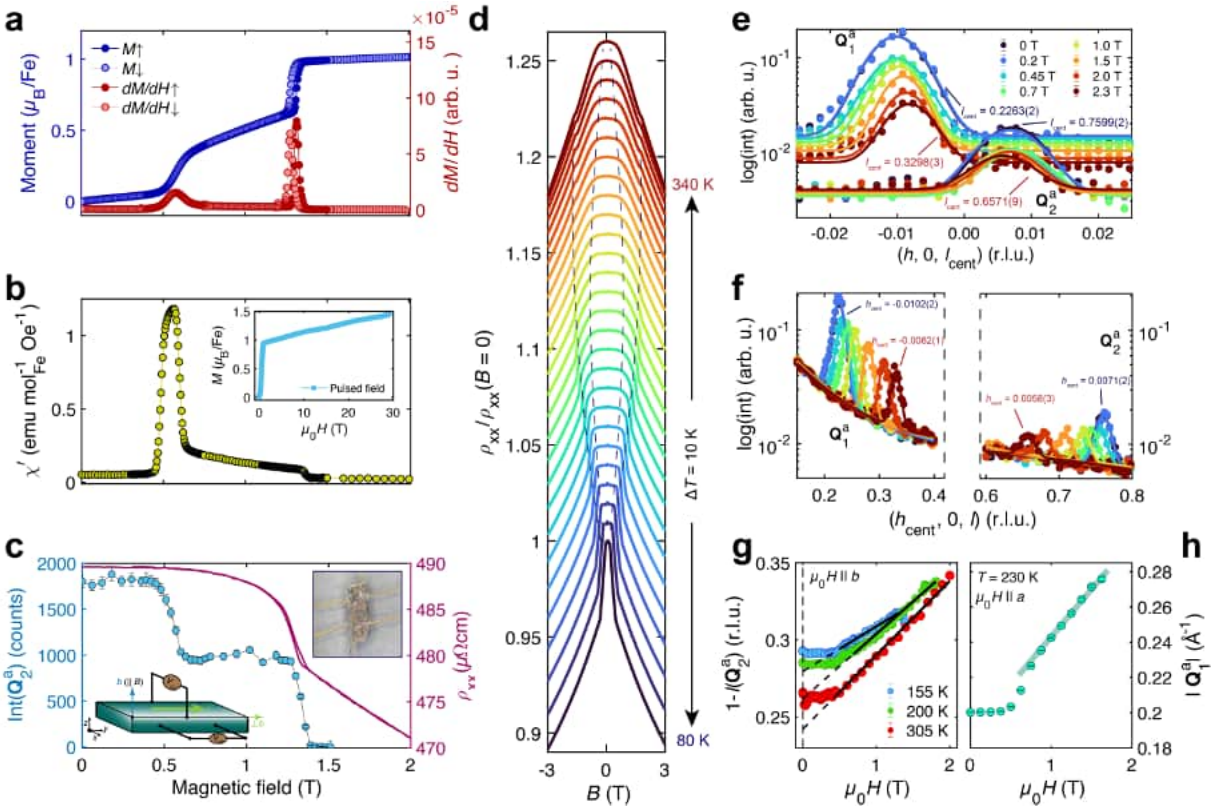

FIG. 3. **Helical spiral transformation for in-plane magnetic field. a,** Magnetic moment as a function of applied field at $T = 155$ K is compared with the corresponding dM/dH curve. A small hysteresis is observed at H_{c2}. **b,** Real part of the ac susceptibility (χ') data shows a clear transition at H_{c1} and a weak step-like feature at H_{c2}. The inset shows increasing magnetisation in the $M(H)$ curve obtained at the pulsed field facility up to 30 T at $T = 10$ K. **c,** Magnetic field dependence of the $\mathbf{Q}_2^a = (0.01, 0.00, 0.72)$ intensity and the longitudinal resistance (ρ_{xx}) at $T = 155$ K. Inset shows the plate-type crystal used for electrical transport measurements. **d,** Longitudinal magnetoresistance measured in Phase III of Fe_3Ga_4 between 80 K and 340 K at every 10 K as a function of internal field B. The dashed lines represent phase boundaries corresponding to H_{c1} and H_{c2}. A constant offset of 0.01 is applied between successive curves for better visualisation. Magnetic field variation of the **e,** h- and **f,** l- components of the $\mathbf{Q}_1^a$ and $\mathbf{Q}_2^a$ ICM reflections. **g,** and **h,** show the q_z changes with respect to applied magnetic field for the $\mathbf{Q}_2^a$ and $\mathbf{Q}_1^a$ reflections, respectively. In the region between H_{c1} and H_{c2} the q_z changes were fitted for all three temperatures with straight lines, they were extended (dotted lines) down to $\mu_0 H = 0$ T. Data shown in Panels-(e) to (g) were measured at $T = 255$ K, whereas for panel-h $T = 230$ K.

a competition between the q_z=1/3 and q_z=1/2 propagation vectors.

Next we evidence the existence of a finite topological Hall resistivity ($\rho_{\rm THE}$) through a comparison between the transverse component of resistivity data (ρ_{yx}) with corresponding isothermal magnetisation data presented in Fig. 4a & b. The extraction of $\rho_{\rm THE}$ is explained in more details

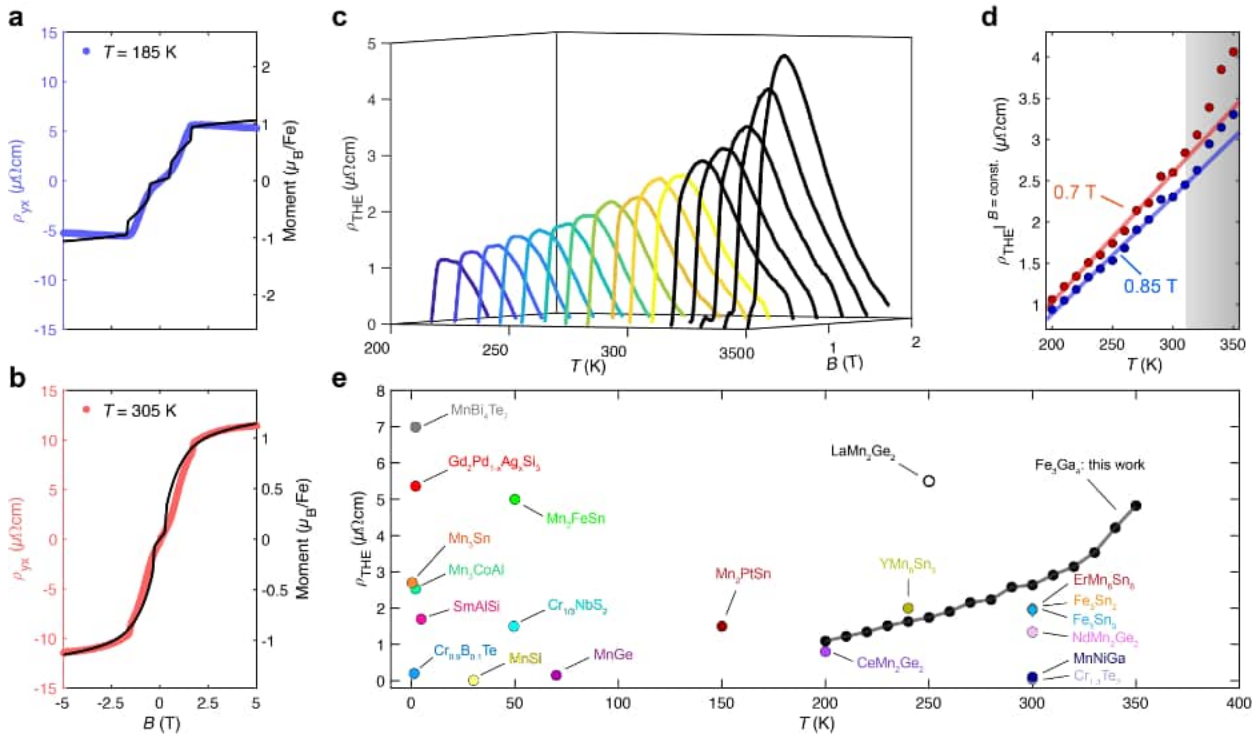

FIG. 4. **Fluctuation-induced topological Hall effect in the transverse conical spiral state.** Comparison between Hall resistivity (ρ_{yx}) and magnetisation data at **a,** 185 K and **b,** 305 K. **c,** Geometrical contribution ($\rho_{\rm THE}$) to the total Hall resistivity shown as a function of magnetic field between 200 K and 350 K, after subtracting the normal and anomalous contributions. **d,** $\rho_{\rm THE}$ as a function of temperature at two constant magnetic fields. The data were fitted with a linear function in Phase IV. Deviation from the linear behavior, marked by shaded region signifies the appearance of Phase V. **e,** Comparison between maximum of topological Hall resistivity ($\rho_{\rm THE}$) in various bulk magnets, among which some even host, as opposed to Fe_3Ga_4, skyrmion lattices. Data shown in panel-e are taken from Refs [9, 10, 17, 21, 28–43].

in the supplementary material. As shown in Fig. 4c, we observe a proportionate increase in $\rho_{\rm THE}$ at elevated temperatures, corresponding to growing fraction of Phase IV in our magnetic phase diagram (see Fig. 1c).

From the quantitative assessment shown in Fig. 4d, we observe a T-linear increase in $|\rho_{\rm THE}|$, strongly supporting the fluctuation-based mechanism of THE. The magnitude of $\rho_{\rm THE}$ observed in Fe_3Ga_4 matches that arising from the short-periodic topologically protected spin textures, such as a skyrmion lattice (SkL) phase [9, 12]. But, unlike in these magnets, THE observed in Fe_3Ga_4 is generated by a single-**k** incommensurate magnetic structure, at room temperature.

DISCUSSION

Our experimental findings on Fe_3Ga_4 , particularly the SND and SNP results, reveal crucial details of both high-temperature Phases III, IV, as well as low-temperature Phases I, II. This allows us to speculate about the main components of the exchange Hamiltonian of the system and to propose the origin of the observed THE in Phase IV.

The propagation vector of Phase III has two incommensurate components, q_z along c^* ($\gamma \approx$ 0.27) and q_x along a^* ($\alpha \approx$ -0.01). The experimental behaviour of the $\gamma \approx 0.27$ component in Phase III is already highlighted in the previous section, here we discuss its theoretical validation. Non-relativistic spiral spin calculations [25] favor magnetic orders with propagation vectors along the (0 0 q_z) direction over the general (q_x q_y q_z) solutions, with a shallow energy minimum at q_z= 0.27. These calculations predict that the observed commensurate propagation vector q_z= 0.5 of Phase I is higher in energy than the incommensurate vector of Phase III with q_z= 0.27. However, antiferromagnetic cell doubling is much more favorable than the ferromagnetic ground state proposed in Ref. [26]. Spiral calculations are not possible with spin-orbit coupling (SOC), since the generalized Bloch theorem is not applicable [44]. Therefore, we performed calculations with SOC in a quadrupled supercell, using the same computational setup as in Ref. [25], thus accessing three energies: for $q_z = 0$, 0.25 and 0.5. The results are shown in Figure S5. The energy difference between the two latter cases is reduced from 1.12 meV/Fe to 0.45 meV/Fe ($\approx$ 5 K). Still, the calculated energy of the $q_z = 0.5$ state is higher than $q_z = 0.25$. Thus ,the realised state with $q_z = 0.5$ is supported by factors not captured by DFT calculations. Such factors could include subtle structural changes accompanying the first-order magnetic transition from Phase III to Phase I.

In Phase I our neutron scattering experiments identified Fe-slabs with the Fe moments being parallel within the slabs stacked along c, while the moments of adjacent slabs are opposite. These slabs were highlighted already in the structural unit cell in Fig.1 and their stacking in the magnetic unit cell is shown in Fig.S6. Such arrangement suggests strong (and predominantly) ferromagnetic intra-layer couplings combined with weaker antiferromagnetic inter-slab exchanges. We speculate that this competition at elevated temperatures leads to an incommensurate twist between the magnetic moments in the slabs.

It is important to note that our SNP results unambiguously prove that the ICM order in Phase III is chiral, contrary to Ref. [26], but in agreement with Ref. [25], while the population of two chiral domains is non-equal, the last being unexpected for a centrosymmetric structure. Similar nontrivial chiral properties were observed in YMn_6Sn_6 [45] and we suspect that in both cases this

population imbalance (and possibly tiny α-component in Fe_3Ga_4) is caused by strains or disorder discussed in Refs.[22, 46], which we observed as a reduction in crystal quality on rapid cooling at low temperatures. The tiny α-component is an unexpected experimental outcome and its significance should still be understood. One possibility is that local variations in the structure allow for symmetry breaking between Fe-Fe bonds, which could generate a finite DMI.

Our experiments show that the q_z component changes abruptly with the field when passing from Phase III to Phase IV. This indicates that the change is likely related to the canting of the cycloidal TCS spiral, which is approximately linear in the field. The change of q_z is significant (almost 20%) within Phase IV for both reflections $\mathbf{Q}_1^{\mathrm{a}}$ and $\mathbf{Q}_2^{\mathrm{a}}$ (Fig. S7e). The increase is steeper at higher temperatures, suggesting the importance of thermal fluctuations. This behaviour is similar to YMn_6Sn_6 [45], wherein an in-plane magnetic field flops the helical spiral into the transverse conical one, that is a cycloid with a net moment component orthogonal to the plane of rotation. Concomitantly, a discontinuous change in q_z is observed, albeit noticeably smaller than in Fe_3Ga_4 . For isotropic (Heisenberg) exchange systems the spiral pitch and subsequently the length of $\mathbf{q}$ is determined by frustration of exchange parameters and is independent of the spin-rotation plane. Another common parameter, single-ion anisotropy, also does not affect the length of $\mathbf{q}$. However, anisotropic exchange terms, such as $J^z S_1^z S_2^z$, can influence the magnitude of the propagation vector. In YMn_6Sn_6, where the Hamiltonian is much simpler, DFT calculations of J_z quantitatively matches the observed jump of q_z. In Fe_3Ga_4 , the exchange network is too complicated to attempt such calculations. However, based on the changes in q_z observed experimentally, we anticipate that anisotropic exchange interactions are present and likely are quite strong.

As mentioned, when a magnetic field is applied to a spiral state within the spiral plane, the moments flop into the TCS state, which is a combination of a cycloid orthogonal to the field and a net moment component (see Fig.1a). The emergent magnetic field $\mathcal{B}$ within the TCS phase is zero and therefore no THE should exist. However, according to the fluctuation-based mechanism [19], the excitation probability of spin waves with opposite chirality is unequal, resulting in a non-zero $\mathcal{B}$ at finite T within the TCS phase. This emergent magnetic field is linearly dependent on temperature and field, and quadratically dependent on net magnetisation. The experimental measured quantity is the topological Hall resistivity which is proportional to $\mathcal{B}$. As discussed above, Fe_3Ga_4 satisfies all the prerequisites for the topological Hall signal generated by the dynamical effects in Phase IV. Also, $|\rho_{\mathrm{THE}}|$ is maximized in Phase V, indicating a possible non-trivial spin configuration. Since Fe_3Ga_4 belongs to a highly tuneable family of Fe-Ga alloys, our results open up attractive potential applications at room temperature. Some of these routes include, but are not limited to, emergent

electromagnetic induction [47], uniaxial strain engineering, and dynamical Berry phase tuning [9] though precise chemical substitution, among others.

METHODS

Single crystal growth and characterisations:

Fe_3Ga_4 single crystal samples were grown by chemical vapor transport (CVT) method using iodine as the transport agent. Stoichiometric amount of Fe powder and Ga ingots, together with 250 mg of iodine were sealed inside a quartz ampoule of inner diameter 4 cm and length about 20 cm. The ampule was placed inside a two-zone furnace while the temperature of source and sink side were maintained at 550 °C and 500 °C, respectively. After two weeks of transport, the ampule was quenched to ice-cold water. The resultant crystals had a needle shape morphology with the long axis along b. All experiments mentioned in this article were performed on needle-type crystals, except for transport measurements which were carried out on a rectangular plate-like crystal.

Quality and structure of all single crystalline specimens used in this study were verified using single crystal X-ray diffraction prior to other measurements. Single crystals were mounted on the goniometer head fitted with a cryo-loop. Data collection was performed on a Rigaku Synergy-I XtaLAB Xray diffractometer, equipped with a Mo micro-focusing source ($\lambda_{k\alpha}$ = 0.71073 Å) and a HyPix-3000 Hybrid Pixel Array detector (Bantam). Data reduction and absorption were carried out with CrysAlisPro and structure was solved and refined with ShelX package within OLEX2 software.

Magnetisation, susceptibility and electrical transport measurements:

Magnetometry studies were performed using commercial 14T PPMS and MPMS3 from Quantum Design (QD). Except for measuring magnetisation under azimuthal rotation, needle-type single crystal was fixed on a quartz sample holder with the b-axis along the direction of magnetic field. Further for the $M(\psi)$ measurements, in order to access both ac and a^*b rotational planes, two types of rotors provided by QD were utilized. The same single crystal sample was fixed in the rotation center with a tiny amount of GE varnish.

Electrical transport measurements were performed using the transport option of the same 14T PPMS. The plate-type single crystal was mounted on a sapphire plate with six contacts (two longitudinal and four transverse). For Hall effect measurements, magnetic field was stabilized at each point prior to data collection.

Single crystal neutron diffraction experiments:

Several neutron diffraction experiments were performed on the single crystal constant-wavelength diffractometers ZEBRA, DMC (SINQ, PSI) and time-of-flight instrument WISH (ISIS, RAL). The dataset at 10 K in zero field was collected on ZEBRA in a cooling machine with the 4-circle setup. Diffraction experiments in magnetic field were performed at all three diffractometers using normal beam geometry. Two different 10 T vertical magnets were used at WISH and SINQ (DMC & ZEBRA). The wavelengths used on DMC were 2.45 Å and 4.52 Å, while those on ZEBRA were 1.383 Å and 2.31 Å. The same needle-shaped single crystal (with [010] axis vertical) was used for all these experiments. The quality of the crystal was deteriorating on fast cooling but then recovering on heating to room temperature. This is the reason why some scans show multiple peaks originating from crystallites $circa$ 2 deg apart.

Small Angle Neutron Scattering (SANS) measurements:

To track the temperature and field dependence of the ICM satellites, SANS studies were conducted using two instruments: D33 at the Institut Laue Langevin (ILL) and SANS-I at SINQ, PSI. For both experiments, a needle-type single crystal was aligned with the b-axis vertical (offset $\sim$ 0.6 deg) on an Al-plate, providing access to the $(h0l)$ scattering plane.

For the SANS experiments performed on D33, neutrons with wavelength λ = 4.6 Å with a spread ($\Delta\lambda/\lambda$) of 10% were used. The neutron beam was collimated at a distance of 2.8 m before the sample, while the main (side) detector was placed 2 m (1.2 m) behind the sample.

For the second SANS experiment performed on SANS-I, neutrons with wavelength λ = 5 Å and a similar wavelength spread were used. Neutron collimation distance and sample-detector distances were fixed at 4.5 m and 1.85 m, respectively. All SANS data analysis were performed using the GRASP software package [48].

Spherical neutron polarimetry (SNP) measurements:

SNP experiment was carried out with the CRYOPAD setup on the hot neutron diffractometer D3 at the ILL. Similar to unpolarised neutron diffraction experiments, the needle-shaped single crystal was aligned with the [010] axis vertical, giving access to the $(h0l)$ scattering plane, see Fig. 4. Neutrons with the longest available wavelength of 0.843 Å selected by a Cu_2MnAl Heusler monochromator were used. In order to minimize beam depolarisation due to any external magnetic field, sample was positioned inside pair of cryogenically cooled Meissner shields. While the beam polarisation was controlled with a combination of nutator and precession coils, analysis of the outgoing neutron beam was performed by a field-polarized ^{3}He spin filter cell, before finally

being measured with a ^{3}He detector. The final polarisation of the outgoing beam was corrected with respect to the cell efficiency.

[1] Y. Tokura, K. Yasuda, and A. Tsukazaki, Magnetic topological insulators, Nature Reviews Physics **1**, 126 (2019).

[2] N. Nagaosa, T. Morimoto, and Y. Tokura, Transport, magnetic and optical properties of Weyl materials, Nature Reviews Materials **5**, 621 (2020).

[3] Y. Tokura, M. Kawasaki, and N. Nagaosa, Emergent functions of quantum materials, Nature Physics **13**, 1056 (2017).

[4] N. Nagaosa, J. Sinova, S. Onoda, A. H. MacDonald, and N. P. Ong, Anomalous Hall effect, Rev. Mod. Phys. **82**, 1539 (2010).

[5] N. Verma, Z. Addison, and M. Randeria, Unified theory of the anomalous and topological Hall effects with phase-space berry curvatures, Science Advances **8**, eabq2765 (2022).

[6] N. Nagaosa and Y. Tokura, Topological properties and dynamics of magnetic skyrmions, Nature Nanotechnology **8**, 899 (2013).

[7] W. Jiang, X. Zhang, G. Yu, W. Zhang, X. Wang, M. Benjamin Jungfleisch, J. E. Pearson, X. Cheng, O. Heinonen, K. L. Wang, *et al.*, Direct observation of the skyrmion Hall effect, Nature Physics **13**, 162 (2017).

[8] W. Kang, Y. Huang, X. Zhang, Y. Zhou, and W. Zhao, Skyrmion-electronics: An overview and outlook, Proceedings of the IEEE **104**, 2040 (2016).

[9] M. Hirschberger, L. Spitz, T. Nomoto, T. Kurumaji, S. Gao, J. Masell, T. Nakajima, A. Kikkawa, Y. Yamasaki, H. Sagayama, H. Nakao, Y. Taguchi, R. Arita, T.-h. Arima, and Y. Tokura, Topological nernst effect of the two-dimensional skyrmion lattice, Phys. Rev. Lett. **125**, 076602 (2020).

[10] A. Neubauer, C. Pfleiderer, B. Binz, A. Rosch, R. Ritz, P. G. Niklowitz, and P. Böni, Topological Hall effect in the A-phase of MnSi, Phys. Rev. Lett. **102**, 186602 (2009).

[11] N. Kanazawa, M. Kubota, A. Tsukazaki, Y. Kozuka, K. S. Takahashi, M. Kawasaki, M. Ichikawa, F. Kagawa, and Y. Tokura, Discretized topological Hall effect emerging from skyrmions in constricted geometry, Phys. Rev. B **91**, 041122 (2015).

[12] T. Kurumaji, T. Nakajima, M. Hirschberger, A. Kikkawa, Y. Yamasaki, H. Sagayama, H. Nakao, Y. Taguchi, T. hisa Arima, and Y. Tokura, Skyrmion lattice with a giant topological Hall effect in a frustrated triangular-lattice magnet, Science **365**, 914 (2019).

[13] M. Hirschberger, T. Nakajima, S. Gao, L. Peng, A. Kikkawa, T. Kurumaji, M. Kriener, Y. Yamasaki, H. Sagayama, H. Nakao, *et al.*, Skyrmion phase and competing magnetic orders on a breathing kagomé lattice, Nature Communications **10**, 5831 (2019).

[14] N. D. Khanh, T. Nakajima, X. Yu, S. Gao, K. Shibata, M. Hirschberger, Y. Yamasaki, H. Sagayama, H. Nakao, L. Peng, *et al.*, Nanometric square skyrmion lattice in a centrosymmetric tetragonal magnet, Nature Nanotechnology **15**, 444 (2020).

[15] R. Takagi, N. Matsuyama, V. Ukleev, L. Yu, J. S. White, S. Francoual, J. R. Mardegan, S. Hayami, H. Saito, K. Kaneko, *et al.*, Square and rhombic lattices of magnetic skyrmions in a centrosymmetric binary compound, Nature Communications **13**, 1472 (2022).

[16] H. Yoshimochi, R. Takagi, J. Ju, N. Khanh, H. Saito, H. Sagayama, H. Nakao, S. Itoh, Y. Tokura, T. Arima, *et al.*, Multistep topological transitions among meron and skyrmion crystals in a centrosymmetric magnet, Nature Physics , 1 (2024).

[17] N. Kanazawa, Y. Onose, T. Arima, D. Okuyama, K. Ohoyama, S. Wakimoto, K. Kakurai, S. Ishiwata, and Y. Tokura, Large topological Hall effect in a short-period helimagnet MnGe, Phys. Rev. Lett. **106**, 156603 (2011).

[18] Y. Fujishiro, N. Kanazawa, T. Nakajima, X. Yu, K. Ohishi, Y. Kawamura, K. Kakurai, T. Arima, H. Mitamura, A. Miyake, *et al.*, Topological transitions among skyrmion-and hedgehog-lattice states in cubic chiral magnets, Nature communications **10**, 1059 (2019).

[19] N. J. Ghimire, R. L. Dally, L. Poudel, D. C. Jones, D. Michel, N. T. Magar, M. Bleuel, M. A. McGuire, J. S. Jiang, J. F. Mitchell, J. W. Lynn, and I. I. Mazin, Competing magnetic phases and fluctuation-driven scalar spin chirality in the kagome metal YMn_6Sn_6, Science Advances **6**, eabe2680 (2020).

[20] H. Zhang, C. Liu, Y. Zhang, Z. Hou, X. Fu, X. Zhang, X. Gao, and J. Liu, Magnetic field-induced nontrivial spin chirality and large topological Hall effect in kagome magnet $ScMn_6Sn_6$, Applied Physics Letters **121** (2022).

[21] K. Fruhling, A. Streeter, S. Mardanya, X. Wang, P. Baral, O. Zaharko, I. I. Mazin, S. Chowdhury, W. D. Ratcliff, and F. Tafti, Topological Hall effect induced by chiral fluctuations in $ErMn_6Sn_6$, Phys. Rev. Mater. **8**, 094411 (2024).

[22] J. H. Mendez, C. E. Ekuma, Y. Wu, B. W. Fulfer, J. C. Prestigiacomo, W. A. Shelton, M. Jarrell, J. Moreno, D. P. Young, P. W. Adams, A. Karki, R. Jin, J. Y. Chan, and J. F. DiTusa, Competing magnetic states, disorder, and the magnetic character of Fe_3Ga_4, Phys. Rev. B **91**, 144409 (2015).

[23] S. S. Samatham and K. Suresh, Weak arrest-like and field-driven first order magnetic phase transitions of itinerant Fe_3Ga_4 revealed by magnetization and magnetoresistance isotherms, Journal of Magnetism and Magnetic Materials **422**, 174 (2017).

[24] M. Philippe, B. Malaman, B. Roques, A. Courtois, and J. Protas, Structures cristallines des phases Fe_3Ga_4 et Cr_3Ga_4, Acta Crystallographica Section B: Structural Crystallography and Crystal Chemistry **31**, 477 (1975).

[25] M. Afshar and I. I. Mazin, Spin spiral and topological Hall effect in Fe_3Ga_4, Phys. Rev. B **104**, 094418 (2021).

[26] Y. Wu, Z. Ning, H. Cao, G. Cao, K. A. Benavides, S. Karna, G. T. McCandless, R. Jin, J. Y. Chan, W. Shelton, *et al.*, Spin density wave instability in a ferromagnet, Scientific Reports **8**, 5225 (2018).

[27] B. Wilfong, A. Fedorko, D. R. Baigutlin, O. N. Miroshkina, X. Zhou, G. M. Stephen, A. L. Friedman, V. Sharma, O. Bishop, R. Barua, *et al.*, Helical spin ordering in room-temperature metallic antiferromagnet Fe_3Ga_4, Journal of Alloys and Compounds **917**, 165532 (2022).

[28] C. Sürgers, G. Fischer, P. Winkel, and H. V. Löhneysen, Large topological Hall effect in the non-collinear phase of an antiferromagnet, Nature Communications **5**, 3400 (2014).

[29] J. Liu, S. Zuo, J. Shen, Y. Zhang, Z. Li, X. Gao, H. Kang, T. Zhao, F. Hu, J. Sun, *et al.*, Large topological Hall effect and in situ observation of magnetic domain structures in the Mn_2FeSn compound, Materials Today Physics **29**, 100871 (2022).

[30] W. Wang, Y. Zhang, G. Xu, L. Peng, B. Ding, Y. Wang, Z. Hou, X. Zhang, X. Li, E. Liu, *et al.*, A centrosymmetric hexagonal magnet with superstable biskyrmion magnetic nanodomains in a wide temperature range of 100-340K, Advanced Materials **28**, 6887 (2016).

[31] S. Roychowdhury, S. Singh, S. N. Guin, N. Kumar, T. Chakraborty, W. Schnelle, H. Borrmann, C. Shekhar, and C. Felser, Giant topological Hall effect in the noncollinear phase of two-dimensional antiferromagnetic topological insulator $MnBi_4Te_7$, Chemistry of Materials **33**, 8343 (2021).

[32] Q. Wang, Q. Yin, and H. Lei, Giant topological Hall effect of ferromagnetic kagome metal Fe_3Sn_2, Chinese Physics B **29**, 017101 (2020).

[33] X. Zheng, X. Zhao, J. Qi, X. Luo, S. Ma, C. Chen, H. Zeng, G. Yu, N. Fang, S. U. Rehman, *et al.*, Giant topological Hall effect around room temperature in noncollinear ferromagnet $NdMn_2Ge_2$ single crystal, Applied Physics Letters **118** (2021).

[34] C. Zhang, C. Liu, J. Zhang, Y. Yuan, Y. Wen, Y. Li, D. Zheng, Q. Zhang, Z. Hou, G. Yin, *et al.*, Room-Temperature magnetic skyrmions and large topological Hall effect in chromium telluride engineered by self-intercalation, Advanced Materials **35**, 2205967 (2023).

[35] Z. Liu, A. Burigu, Y. Zhang, H. M. Jafri, X. Ma, E. Liu, W. Wang, and G. Wu, Giant topological Hall effect in tetragonal Heusler alloy Mn_2PtSn, Scripta Materialia **143**, 122 (2018).

[36] X. Yao, J. Gaudet, R. Verma, D. E. Graf, H.-Y. Yang, F. Bahrami, R. Zhang, A. A. Aczel, S. Subedi, D. H. Torchinsky, J. Sun, A. Bansil, S.-M. Huang, B. Singh, P. Blaha, P. Nikolić, and F. Tafti, Large topological Hall effect and spiral magnetic order in the Weyl semimetal SmAlSi, Phys. Rev. X **13**, 011035 (2023).

[37] P. K. Rout, P. V. P. Madduri, S. K. Manna, and A. K. Nayak, Field-induced topological Hall effect in the noncoplanar triangular antiferromagnetic geometry of Mn_3Sn, Phys. Rev. B **99**, 094430 (2019).

[38] G. Xu, D. Liu, L. He, S. Wang, and L. Ma, A giant topological Hall effect in ferromagnetic compound $CeMn_2Ge_2$ with wide temperature range from 70 to 310 K, Materials Letters **315**, 131963 (2022).

[39] A. E. Hall, J. C. Loudon, P. A. Midgley, A. C. Twitchett-Harrison, S. J. R. Holt, D. A. Mayoh, J. P. Tidey, Y. Han, M. R. Lees, and G. Balakrishnan, Comparative study of the structural and magnetic properties of $Mn_{1/3}NbS_2$ and $Cr_{1/3}NbS_2$, Phys. Rev. Mater. **6**, 024407 (2022).

[40] Y. He, J. Kroder, J. Gayles, C. Fu, Y. Pan, W. Schnelle, C. Felser, and G. H. Fecher, Large topological Hall effect in an easy-cone ferromagnet $(Cr_{0.9}B_{0.1})Te$, Applied Physics Letters **117** (2020).

[41] H. Li, B. Ding, J. Chen, Z. Li, E. Liu, X. Xi, G. Wu, and W. Wang, Large anisotropic topological Hall

effect in a hexagonal non-collinear magnet Fe_5Sn_3, Applied Physics Letters **116** (2020).

[42] Q. Wang, K. J. Neubauer, C. Duan, Q. Yin, S. Fujitsu, H. Hosono, F. Ye, R. Zhang, S. Chi, K. Krycka, H. Lei, and P. Dai, Field-induced topological Hall effect and double-fan spin structure with a c-axis component in the metallic kagome antiferromagnetic compound YMn_6Sn_6, Phys. Rev. B **103**, 014416 (2021).

[43] S. Roychowdhury, P. Yanda, K. Samanta, C. Yi, M. Yao, F. Orlandi, P. Manuel, D. Khalyavin, E. G. D. Valle, P. Constantinou, *et al.*, Giant room-temperature topological Hall effect in a square-net ferromagnet $LaMn_2Ge_2$, Advanced Materials , 2305916 (2024).

[44] L. M. Sandratskii, Energy band structure calculations for crystals with spiral magnetic structure, physica status solidi (b) **136**, 167 (1986).

[45] R. L. Dally, J. W. Lynn, N. J. Ghimire, D. Michel, P. Siegfried, and I. I. Mazin, Chiral properties of the zero-field spiral state and field-induced magnetic phases of the itinerant kagome metal YMn_6Sn_6, Phys. Rev. B **103**, 094413 (2021).

[46] B. Wilfong, V. Sharma, J. Naphy, O. Bishop, S. P. Bennett, J. Prestigiacomo, R. Barua, and M. E. Jamer, Altering the magnetic ordering of Fe_3Ga_4 via thermal annealing and hydrostatic pressure, Journal of Alloys and Compounds **894**, 162421 (2022).

[47] T. Yokouchi, F. Kagawa, M. Hirschberger, Y. Otani, N. Nagaosa, and Y. Tokura, Emergent electromagnetic induction in a helical-spin magnet, Nature **586**, 232 (2020).

[48] C. Dewhurst, Graphical reduction and analysis small-angle neutron scattering program: GRASP, Journal of Applied Crystallography **56** (2023).

[49] J. Perez-Mato, S. Gallego, E. Tasci, L. Elcoro, G. de la Flor, and M. Aroyo, Symmetry-based computational tools for magnetic crystallography, Annual Review of Materials Research **45**, 217 (2015).

[50] P. R. Baral, O. I. Utesov, C. Luo, F. Radu, A. Magrez, J. S. White, and V. Ukleev, Direct observation of exchange anisotropy in the helimagnetic insulator Cu_2OSeO_3, Phys. Rev. Res. **5**, L032019 (2023).

DATA AVAILABILITY

All neutron scattering data will be available via their corresponding DOIs.

ACKNOWLEDGEMENTS

Swiss National Science Foundation (SNSF) projects, Sinergia Network “NanoSkyrmionics” grant no. CRSII5_171003 (P.R.B., V.U., A.M., & J.S.W.), 200021_188707 (P.R.B., V.U., & J.S.W.), and 200020_182536 (P.R.B. & O.Z.), are acknowledged for financial assistance. I.I.M. was partially supported by the National Science Foundation under Award No. DMR-2403804. We acknowledge beamtime allocation from PSI (20202357, 20230062, 20230040), ILL (DIR-241, 5-54-409), ISIS-RAL (2220587) and HLD-HZDR (member of the European Magnetic Field Laboratory (EMFL)) facilities. This work is based partly on experiments performed at the Swiss spallation neutron

source SINQ, Paul Scherrer Institute, Villigen, Switzerland. We thank Dr. Wen Hua Bi for his assistance with the single crystal X-ray diffraction experiments.

AUTHOR CONTRIBUTIONS

P.R.B. and A.M. grew the single crystals and characterized them. P.R.B., I.Ž., and Y.L. performed the magnetometry and transport measurements. High-field measurements were performed by P.R.B., Y.S., and O.Z. Neutron diffraction measurements were performed by P.R.B., V.U., F.O., P.M., L.K., and O.Z. Spherical neutron polarimetry experiments were performed by P.R.B., A.S., J.A.R., and O.Z. P.R.B., V.U., R.C. and J.S.W. performed the small angle neutron scattering measurements. Data analysis was performed by P.R.B. and O.Z. I.I.M. provided the theoretical interpretation. The manuscript was written by P.R.B. and O.Z., with input from I.I.M. All coauthors read and commented on the draft. P.R.B., V.U., and O.Z. conceived the project.

COMPETING INTERESTS

The authors declare no competing financial interests.

Supplementary information for

"Fluctuation-driven topological Hall effect in room-temperature itinerant helimagnet Fe_3Ga_4 "

The supplementary materials contain additional information concerning single crystal X-ray diffraction, magnetisation, ac susceptibility, neutron diffraction, small angle neutron scattering as well as spherical neutron polarimetry data to support the results presented in the main text.

I. SINGLE CRYSTAL CHARACTERISATIONS

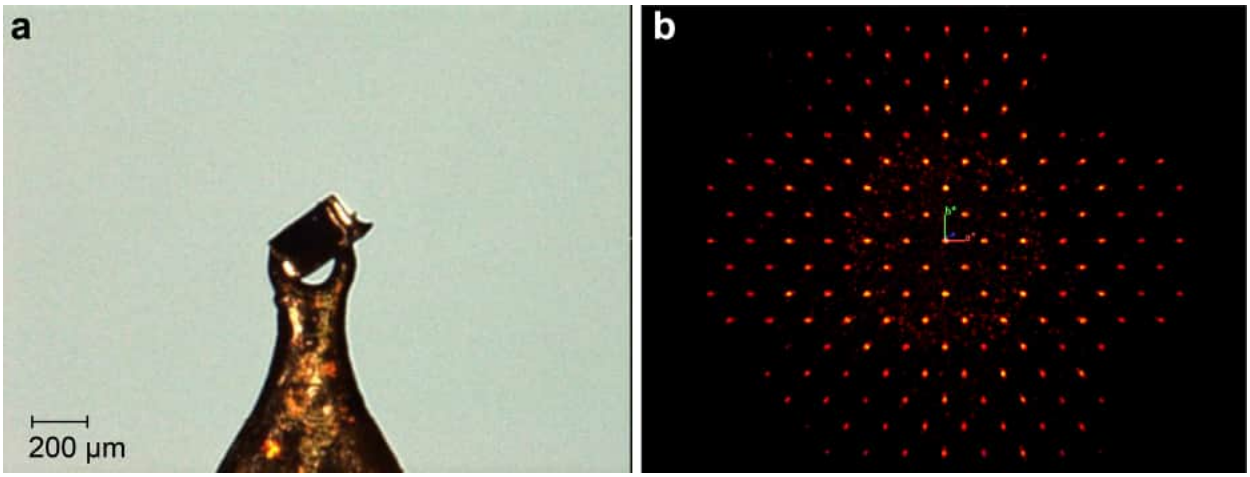

FIG. S1. **Single crystal X-ray diffraction. a**. A small Fe_3Ga_4 single crystal mounted on a holder for X-ray diffraction experiments. **b**. Reciprocal space map obtained at room temperature.

A preliminary quality check was performed on each single crystal sample used for this study via X-ray diffraction experiments both at room temperature as well as at 200 K. Here, we show results from one of our X-ray diffraction experiments. A small Fe_3Ga_4 crystal of size approximately 120 μm was mounted on a needle-type holder. We acquired a total of 2038 reflections to refine the crystal structure at 200 K. The best solution was found for the space group $C2/m$ (#12) with lattice constants as: 10.0966(5) Å, 7.6650(4) Å, 7.8655(4) Å, 90^0, $106.251(4)^0$, and 90^0. This unit cell matches quite well with the previous results [24].

II. BULK MAGNETOMETRY

Magnetisation and ac susceptibility measurements were also performed in Phase I and VI. A linear increase in $M(H)$, and thus a constant dM/dH is observed (in Fig. S2a) in both Phases until the first inflection point. Further we observe a slower increase in magnetisation until 14 T. High-field

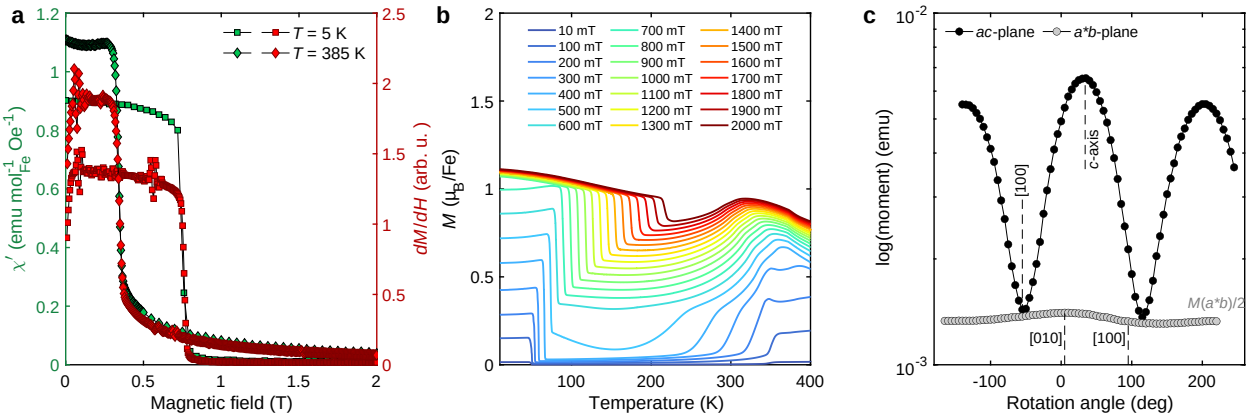

FIG. S2. **Additional magnetometry data on Fe_3Ga_4.**(a) Field evolution of isothermal dynamic ac-susceptibility χ' and static magnetisation M in Phases I and VI at temperatures 5 K and 385 K. (b) Temperature dependent magnetisation of a Fe_3Ga_4 single crystal with a series of constant magnetic fields applied along the b-axis. Each scan was measured between 5 K and 395 K in a sweep mode. (c) Angle dependent magnetisation data for a needle-type Fe_3Ga_4 single crystal measured at $T = 30$ K with 0.05 T constant magnetic field. Two distinct rotation planes, ac- and a^*b-, were selected similar to what is shown in Fig. 2c.

magnetisation measured in Phase I at $T = 10$ K confirms that Fe_3Ga_4 does not attain saturation moment even until 30 T. The temperature scans shown in panel-b of Fig. S2, evidence for previously unreported Phase V and VII is quite clear. Multiple transitions are observed in $M(T)$ curves measured with lowest magnetic fields, for example 100 mT. While the drop observed with $\mu_0 H = 2$ T signifies the transition in and out of Phase IV from its adjacent phases. Magnetisation rotation measurements were also performed in Phase I, similar to the data shown in main text figure 2c. As $m_c > m_a \geq m_b$ was also obtained in Phase I, we can conclude that magnetic anisotropy is similar for both Phases I and III.

III. SPHERICAL NEUTRON POLARIMETRY

Precise directional information about the magnetic order in Fe_3Ga_4 was obtained using the SNP experiment on the hot neutron source (D3) at the ILL. To interpret the data a local coordinate system for each reflection is chosen such that the x-axis is fixed along $\mathbf{Q}$ (shown in Fig. 4a), the z-axis is vertical and y completes the right-handed Cartesian set. For each of the three incoming neutron polarisations P_x^{in}, P_y^{in} and P_z^{in} the three components in the scattered beam $P_{x,y,z}^{\text{out}}$ are analysed generating in total nine components of the resultant polarisation matrix. This matrix contains contributions of all domains scattering to the magnetic reflection and for each domain contains

polarisation vector P'' created during the scattering and polarisation tensor $\tilde{P}$. The polarisation tensor $\tilde{P}$ can be written as:

$$\tilde{P} = \begin{pmatrix} \frac{\mathbf{N}^2 - \mathbf{M}_\perp^2}{I_x} & -\frac{J_{nz}}{I_x} & \frac{J_{ny}}{I_x} \\ \frac{J_{nz}}{I_y} & \frac{\mathbf{N}^2 - \mathbf{M}_\perp^2 + R_{yy}}{I_y} & \frac{R_{yz}}{I_y} \\ -\frac{J_{ny}}{I_z} & \frac{R_{zy}}{I_z} & \frac{\mathbf{N}^2 - \mathbf{M}_\perp^2 + R_{zz}}{I_z} \end{pmatrix}$$

with P_i^{in} changing within the rows and P_j^{out} within the columns ($i, j = x, y, z$). Here $\mathbf{N}$ and $\mathbf{M}_\perp$ are the nuclear structure factor and the magnetic interaction vector, the projection of the magnetic structure factor orthogonal to $\mathbf{Q}$. The off-diagonal elements contain imaginary nuclear-magnetic interference terms J_{ni}=2 **Im**($\mathbf{N}(\mathbf{Q})\mathbf{M}_{\perp i}^*(\mathbf{Q})$), real R_{ij}=2 **Re**($\mathbf{M}_{\perp i}(\mathbf{Q})\mathbf{M}_{\perp j}^*(\mathbf{Q})$), and intensity terms $I_{i=x,y,z}$ are $I_x = \mathbf{N}^2 + \mathbf{M}_\perp^2 + P_x J_{yz}$, $I_{y/z} = \mathbf{N}^2 + \mathbf{M}_\perp^2 + P_{y/z} R_{n(y/z)}$. The polarisation vector P''

$$P'' = \begin{pmatrix} \frac{J_{nz}}{I} \\ \frac{R_{ny}}{I} \\ \frac{R_{nz}}{I} \end{pmatrix}.$$

contains, the so-called magnetic interference terms $J_{ij} = 2\mathbf{Im}(\mathbf{M}_{\perp i}(\mathbf{Q})\mathbf{M}_{\perp j}^*(\mathbf{Q}))$, and the real nuclear-magnetic interference terms $R_{ni} = 2\mathbf{Re}(\mathbf{N}(\mathbf{Q})\mathbf{M}_{\perp i}^*(\mathbf{Q}))$.

To index magnetic reflections identified in our SNP experiments precisely, we compared them with higher resolution results from WISH, ZEBRA and DMC. Below the polarisation matrices for various reflections at different temperatures are listed.

Phase I: T = 10 K

k = 0 reflections

We could differentiate two families of reflections. The family **Q** = (4,0,1), (2,0,3), (2,0,-4), (0,0,4), (-2,0,4), and (-4,0,-1) has $P_{xx} = P_{yy} = P_{zz} = 1$ thus, the reflections are purely nuclear. For the family **Q** = (2,0,1), (2,0,0), (-2,0,3), (-2,0,2), (-4,0,3) and (4,0,-1) the P_{xx} and P_{zz} elements are reduced. This could be due to depolarisation of neutrons by combined effect of the global ferromagnetic contribution along c and of the local ferromagnetic components within the slabs along a. This combined field is along the y-local coordinate axes of this second family of reflections, *i. e.* approximately along (101). The resultant polarisation matrices are:

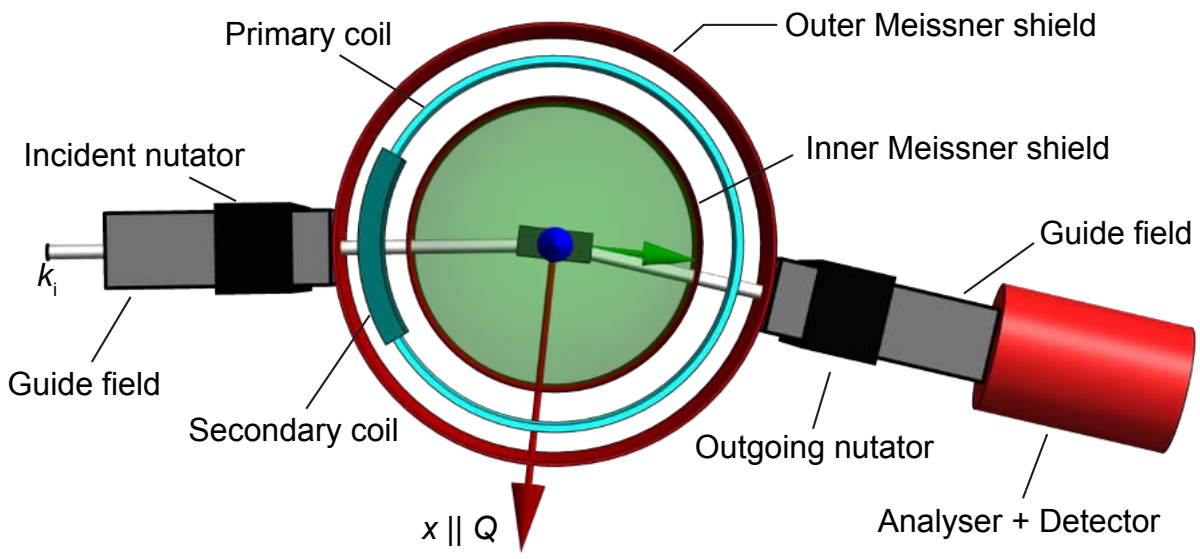

FIG. S3. **Spherical neutron polarimetry experiment using the CRYOPAD setup on D3 (ILL).** Schematics of the CRYOPAD setup used for our SNP experiment on the D3 (ILL) beamline. The single crystal is centered inside two concentric Meissner shields achieving a net zero magnetic field condition. The x-coordinate of the local polarisation axis is chosen such that it coincides with the direction of $\mathbf{Q}$. The remaining local axes (y and z) are chosen in order to satisfy the right hand coordinate system. Using the guide field, the incoming polarisation of the neutron beam is tuned to match one of the local axes of a particular Bragg reflection, while all three components of the outgoing polarisation vector is measured.

1. $\mathbf{Q}$ = (4.0, 0.0, 1.0)

$$\begin{pmatrix} 1.05 \pm 0.14 & 0.04 \pm 0.01 & -0.03 \pm 0.01 \\ -0.06 \pm 0.01 & 1.06 \pm 0.14 & -0.03 \pm 0.01 \\ -0.01 \pm 0.01 & 0.02 \pm 0.01 & 1.01 \pm 0.01 \end{pmatrix}$$

2. $\mathbf{Q}$ = (2.0, 0.0, 3.0)

$$\begin{pmatrix} 0.99 \pm 0.04 & 0.07 \pm 0.06 & -0.02 \pm 0.06 \\ -0.08 \pm 0.06 & 1.05 \pm 0.03 & 0.06 \pm 0.06 \\ 0.04 \pm 0.05 & 0.02 \pm 0.08 & 0.99 \pm 0.03 \end{pmatrix}$$

3. $\mathbf{Q}$ = (2.0, 0.0, 1.0)

$$\begin{pmatrix} 0.78 \pm 0.03 & 0.02 \pm 0.04 & -0.03 \pm 0.04 \\ -0.05 \pm 0.04 & 1.01 \pm 0.03 & 0.04 \pm 0.04 \\ 0.05 \pm 0.04 & -0.03 \pm 0.04 & 0.79 \pm 0.03 \end{pmatrix}$$

4. **Q** = (2.0, 0.0, 0.0)

$$\begin{pmatrix} 0.61 \pm 0.05 & 0.05 \pm 0.05 & -0.04 \pm 0.05 \\ 0.01 \pm 0.05 & 1.12 \pm 0.04 & 0.04 \pm 0.05 \\ 0.01 \pm 0.06 & 0.01 \pm 0.05 & 0.62 \pm 0.04 \end{pmatrix}$$

5. **Q** = (2.0, 0.0, -4.0)

$$\begin{pmatrix} 0.99 \pm 0.03 & -0.02 \pm 0.04 & -0.01 \pm 0.04 \\ -0.02 \pm 0.04 & 1.04 \pm 0.02 & 0.05 \pm 0.04 \\ -0.03 \pm 0.04 & 0.03 \pm 0.04 & 0.99 \pm 0.03 \end{pmatrix}$$

6. **Q** = (0.0, 0.0, 4.0)

$$\begin{pmatrix} 0.99 \pm 0.02 & 0.04 \pm 0.03 & -0.05 \pm 0.03 \\ -0.07 \pm 0.04 & 0.99 \pm 0.02 & 0.06 \pm 0.03 \\ -0.03 \pm 0.04 & 0.07 \pm 0.04 & 0.99 \pm 0.02 \end{pmatrix}$$

7. **Q** = (-2.0, 0.0, 4.0)

$$\begin{pmatrix} 0.99 \pm 0.02 & -0.01 \pm 0.03 & 0.01 \pm 0.03 \\ -0.05 \pm 0.03 & 1.01 \pm 0.02 & -0.05 \pm 0.03 \\ -0.01 \pm 0.03 & 0.05 \pm 0.03 & 1.00 \pm 0.02 \end{pmatrix}$$

8. **Q** = (-2.0, 0.0, 3.0)

$$\begin{pmatrix} 0.85 \pm 0.03 & 0.03 \pm 0.04 & -0.01 \pm 0.04 \\ -0.07 \pm 0.04 & 1.02 \pm 0.03 & -0.04 \pm 0.04 \\ 0.05 \pm 0.04 & -0.05 \pm 0.04 & 0.87 \pm 0.03 \end{pmatrix}$$

9. **Q** = (-2.0, 0.0, 2.0)

$$\begin{pmatrix} 0.38 \pm 0.02 & 0.04 \pm 0.02 & -0.03 \pm 0.02 \\ 0.04 \pm 0.02 & 1.05 \pm 0.02 & -0.05 \pm 0.02 \\ -0.02 \pm 0.02 & 0.01 \pm 0.02 & 0.38 \pm 0.02 \end{pmatrix}$$

10. **Q** = (-4.0, 0.0, 3.0)

$$\begin{pmatrix} 0.80 \pm 0.04 & 0.09 \pm 0.02 & -0.04 \pm 0.03 \\ -0.01 \pm 0.03 & 1.02 \pm 0.06 & -0.02 \pm 0.03 \\ -0.03 \pm 0.03 & -0.01 \pm 0.03 & 0.78 \pm 0.02 \end{pmatrix}$$

11. **Q** = (-4.0, 0.0, -1.0)

$$\begin{pmatrix} 1.02 \pm 0.01 & 0.01 \pm 0.02 & -0.01 \pm 0.02 \\ -0.08 \pm 0.02 & 0.99 \pm 0.01 & 0.01 \pm 0.01 \\ 0.00 \pm 0.01 & 0.05 \pm 0.01 & 1.01 \pm 0.01 \end{pmatrix}$$

12. **Q** = (4.0, 0.0, -1.0)

$$\begin{pmatrix} 0.42 \pm 0.04 & -0.01 \pm 0.04 & -0.02 \pm 0.04 \\ -0.16 \pm 0.04 & 0.94 \pm 0.03 & -0.01 \pm 0.04 \\ -0.03 \pm 0.04 & 0.09 \pm 0.04 & 0.47 \pm 0.04 \end{pmatrix}$$

k = (0 0 1/2) reflections

1. **Q** = (0.0, 0.0, -1/2)

$$\begin{pmatrix} -0.99 \pm 0.03 & -0.03 \pm 0.03 & 0.05 \pm 0.03 \\ 0.01 \pm 0.03 & 0.99 \pm 0.02 & 0.07 \pm 0.02 \\ 0.02 \pm 0.02 & 0.07 \pm 0.03 & -1.00 \pm 0.03 \end{pmatrix}$$

2. **Q** = (0.0, 0.0, 1/2)

$$\begin{pmatrix} -1.02 \pm 0.03 & -0.01 \pm 0.03 & -0.01 \pm 0.03 \\ 0.03 \pm 0.02 & 1.01 \pm 0.03 & -0.10 \pm 0.02 \\ 0.02 \pm 0.04 & -0.09 \pm 0.03 & -1.01 \pm 0.03 \end{pmatrix}$$

Phase III: T = 155 K

k = 0 reflections

1. **Q**= (4.0, 0.0, 1.0)

$$\begin{pmatrix} 1.02 \pm 0.01 & 0.02 \pm 0.02 & -0.03 \pm 0.02 \\ -0.09 \pm 0.02 & 0.99 \pm 0.01 & -0.01 \pm 0.02 \\ -0.02 \pm 0.02 & 0.07 \pm 0.02 & 1.00 \pm 0.01 \end{pmatrix}$$

2. **Q** = (2.0, 0.0, 1.0)

$$\begin{pmatrix} 1.07 \pm 0.05 & 0.04 \pm 0.06 & 0.11 \pm 0.07 \\ -0.11 \pm 0.06 & 0.93 \pm 0.05 & -0.05 \pm 0.06 \\ -0.12 \pm 0.06 & 0.07 \pm 0.07 & 0.96 \pm 0.06 \end{pmatrix}$$

3. $\mathbf{Q}$ = (2.0, 0.0, 0.0)

$$\begin{pmatrix} 0.90 \pm 0.05 & -0.06 \pm 0.05 & -0.03 \pm 0.05 \\ -0.02 \pm 0.06 & 0.97 \pm 0.05 & 0.05 \pm 0.07 \\ -0.01 \pm 0.12 & -0.14 \pm 0.06 & 1.05 \pm 0.05 \end{pmatrix}$$

4. $\mathbf{Q}$ = (-2.0, 0.0, 4.0)

$$\begin{pmatrix} 0.97 \pm 0.02 & -0.01 \pm 0.03 & -0.04 \pm 0.04 \\ -0.04 \pm 0.03 & 0.98 \pm 0.02 & 0.01 \pm 0.03 \\ -0.04 \pm 0.04 & 0.02 \pm 0.04 & 0.97 \pm 0.02 \end{pmatrix}$$

$\mathbf{k} = (\alpha\ 0\ \gamma)$ reflections

5. $\mathbf{Q}_2^{\mathrm{a}}$ = (0.007, 0.00, 0.759)

$$\begin{pmatrix} -1.04 \pm 0.03 & -0.04 \pm 0.06 & -0.01 \pm 0.07 \\ -0.43 \pm 0.05 & 0.01 \pm 0.04 & -0.01 \pm 0.05 \\ -0.48 \pm 0.05 & -0.02 \pm 0.04 & -0.06 \pm 0.05 \end{pmatrix}$$

6. $\mathbf{Q}_1^{\mathrm{b}}$ = (1.99, 0.00, 1.28)

$$\begin{pmatrix} -1.01 \pm 0.22 & -0.01 \pm 0.13 & 0.15 \pm 0.35 \\ 0.37 \pm 0.08 & -0.53 \pm 0.09 & -0.13 \pm 0.17 \\ 0.29 \pm 0.12 & 0.17 \pm 0.21 & 0.34 \pm 0.12 \end{pmatrix}$$

7. -$\mathbf{Q}_2^{\mathrm{a}}$ = (-0.01, 0.00, -0.73)

$$\begin{pmatrix} -1.05 \pm 0.04 & -0.02 \pm 0.04 & -- \\ -0.28 \pm 0.05 & -0.01 \pm 0.06 & -- \\ -0.31 \pm 0.05 & -- & 0.02 \pm 0.05 \end{pmatrix}$$

Phase III: T = 288 K

$\mathbf{k}$ = 0 reflections

1. $\mathbf{Q}$ = (2.0, 0.0, 0.0)

$$\begin{pmatrix} 1.04 \pm 0.17 & 0.03 \pm 0.18 & -0.07 \pm 0.16 \\ -0.32 \pm 0.15 & 0.95 \pm 0.16 & -0.22 \pm 0.16 \\ -0.15 \pm 0.18 & 0.18 \pm 0.19 & 0.94 \pm 0.16 \end{pmatrix}$$

2. $\mathbf{Q}$ = (4.0, 0.0, 1.0)

$$\begin{pmatrix} 1.00 \pm 0.01 & 0.04 \pm 0.01 & -0.01 \pm 0.01 \\ -0.05 \pm 0.01 & 1.01 \pm 0.01 & 0.02 \pm 0.01 \\ -0.01 \pm 0.01 & 0.03 \pm 0.01 & 0.99 \pm 0.01 \end{pmatrix}$$

$\mathbf{k} = (\alpha\ 0\ \gamma)$ reflections

1. -$\mathbf{Q}_1^a$ = (-0.01, 0.00, -0.73)

$$\begin{pmatrix} -1.05 \pm 0.06 & -0.01 \pm 0.06 & -0.07 \pm 0.07 \\ -0.63 \pm 0.07 & 0.02 \pm 0.08 & 0.01 \pm 0.11 \\ -0.81 \pm 0.09 & 0.09 \pm 0.09 & -0.15 \pm 0.09 \end{pmatrix}.$$

Here, red and blue represent the extreme values of general matrix elements, P_{xy}, that is +1 and -1, respectively. While the numbers shown in green are intermediate.

IV. SINGLE CRYSTAL NEUTRON DIFFRACTION (SND) AT BASE TEMPERATURE

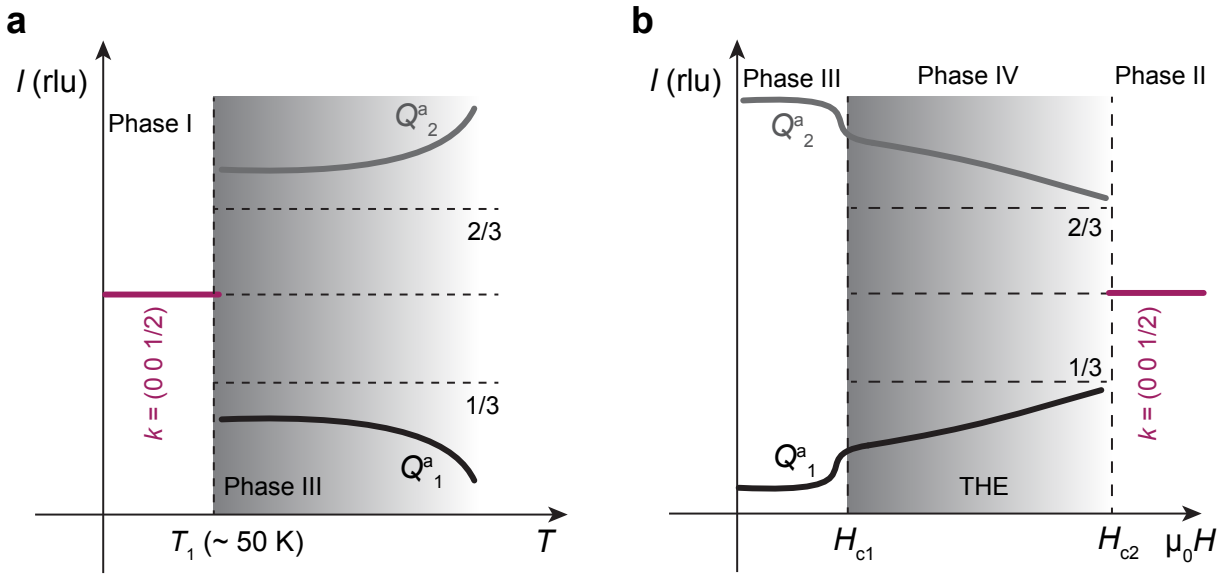

FIG. S4. **Temperature and field dependence of magnetic reflections in Fe_3Ga_4.** Behaviour of ICM reflections together with $\mathbf{Q} = (0, 0, 1/2)$ reflection was reconstructed using results from all the neutron scattering measurements described in the text. Panel-**a** shows the schematics of temperature dependece while magnetic field dependence is shown in Panel-**b**.

The temperature and magnetic field dependencies of the commensurate and incommensurate magnetic reflections obtained by neutron scattering experiments are schematically shown in Fig. S4. The crucial finding from neutron diffraction is the appearance of new magnetic reflections below T_1, which can be indexed with the propagation vector $\mathbf{k} = (0\ 0\ 1/2)$. The commensurate antiferromagnetic state was not detected in previous studies [26]. Figure S6a shows a part of the reciprocal space of Fe_3Ga_4 obtained in Phase I with the WISH diffractometer. The $\mathbf{Q} = (0,0,\pm 1/2)$ reflections are very strong, signaling that magnetic moments lie within the ab-plane. Further, the polarisation matrix measured for the $\mathbf{Q} = (0,0,\pm 1/2)$ reflection on the D3 diffractometer at ILL unambiguously implies that the magnetic moments point along the a-crystal axis: the initial polarisation along the local z-axis (b-crystal axis) flips, while polarisation measured along the y-axis is not changed. A zero field 10 K dataset containing 84 $\mathbf{k} = (0\ 0\ 1/2)$ reflections was collected on the ZEBRA diffractometer. Most of the magnetic reflections were weak and several models from the twelve maximal magnetic space groups proposed by BCS software [49] had similar goodness of fit. We developed the model reconciling results of SND, SNP, and magnetometry. Magnetic moments are constrained to two independent parameters 1.10(6)μ_B/Fe for Fe1, Fe2, Fe3 and 1.47(8)μ_B/Fe for Fe4 in the MSG C2'/c (15.87). The model, in Fig.S6c, comprises ferromagnetic slabs with moments pointing along the a-axis, while neighbouring slabs are aligned opposite to each other.

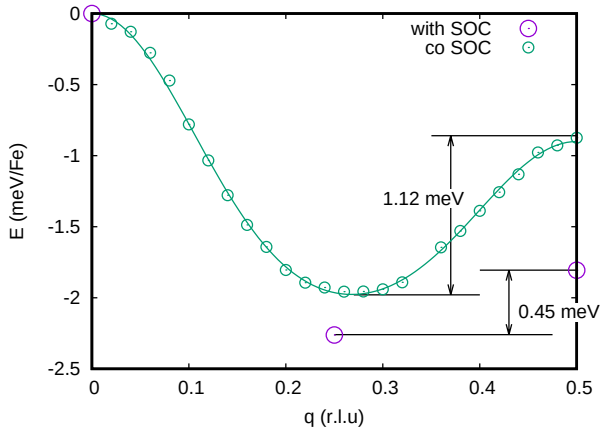

FIG. S5. **Energy landscape of magnetic states.** Energy of various spin states, with and without spin orbit coupling, as a function of q_z obtained from density functional theory calculations.

We observe a narrow coexisting region between Phase I and Phase III around T_1, as shown in Fig. 3a. Below T_1 in zero field, a spontaneous magnetisation develops in Fe_3Ga_4. In our bulk measurements this is witnessed by a rise of magnetisation at T_1 and a hysteresis in the isothermal magnetisation loop. The moment value at 5 K and 10 mT is only 0.15 μ_B/Fe, it steeply increases

till 0.75 T, where is reaches 0.95 μ_B/Fe, and keeps rising at higher fields with moderate increment. Similar moment values are obtained from magnetisation data published by Mendez *et al.* [22] and Wilfong *et al.* [27]. In the single crystal neutron diffraction study of Wu *et al.* [26] the net $\mathbf{k}$=0 moment is assumed to point along the c-axis and the refined value is 1.4(2) μ_B/Fe. We observe the increased intensity of $\mathbf{Q}$ = (2,0,1), similar to Wu *et. al.* [26]. In Phase I, we detect an intriguing reduction of the elements P_{xx} and P_{zz} of the polarization matrices for the reflections $\mathbf{k}$ = 0 located in the zone orthogonal to the [101] direction (Fig. 4b). This reduction most probably arises from depolarisation of the x and z-components by the ferromagnetic contribution, which is along [101], not along c.

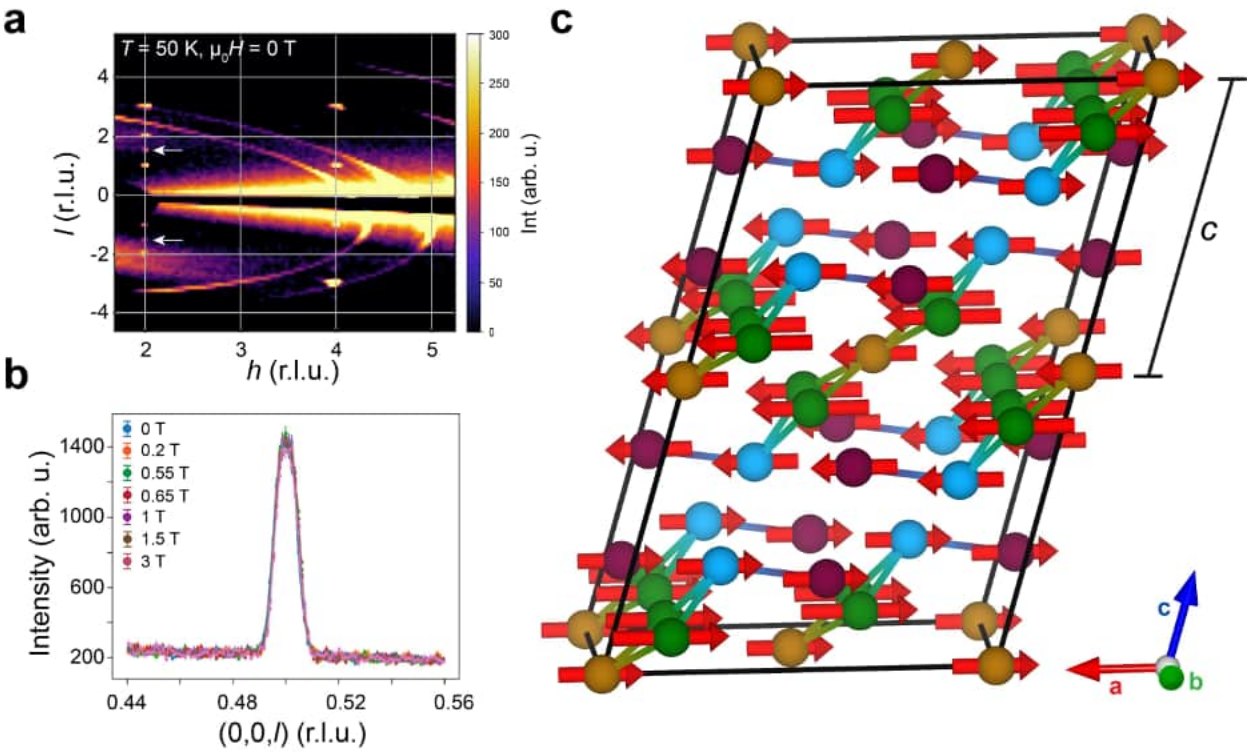

FIG. S6. **Single crystal neutron diffraction in Phase I.** (a) Reciprocal space map for Fe_3Ga_4 obtained in Phase I at 50 K. The white arrows indicate some of the weak (0,0,l) reflections in the ($h0l$) scattering plane. (b) The intensity of the $\mathbf{Q} = (0, 0, 0.5)$ peak was measured with the WISH diffractometer at 50 K, and no noticeable difference was observed up to 3 T magnetic field. (c) Magnetic structure of Fe_3Ga_4 as determined at T = 10 K from single crystal neutron diffraction experiments. Ga-atoms have been removed for clarity. The magnetic unit cell with doubled c comprises two Fe-slabs with magnetic moments along or opposite to the a-axis.

We further identify that the propagation vector $\mathbf{k}$=(0 0 1/2) persists in Phase II. In our diffraction experiment in magnetic field on WISH the intensity of the (0,0,1/2) reflection does not change

in fields from 0 T till 3 T (see Fig. S6b). We presume that $\mathbf{k}$=0 and $\mathbf{k}$=(0 0 1/2) contributions could be combined into an overall ferrimagnetic structure. The magnetisation discontinuity at H_{c1} (0.7 T at 5 K, shown in Fig. S2a) suggests that at H_{c1} the field selection of domains with the favourable ferromagnetic component takes place. The inset of Fig. 2b shows that no further metamagnetic transitions occur till 30 T and magnetisation keeps steadily rising. Thus the canted ferrimagnetic structure with collinear AFM component along a and growing net component along b extends to very high fields, opposite to the presumptions of previous studies. To reach the fully polarised ferromagnetic state fields above 30 T are necessary.

V. SMALL ANGLE NEUTRON SCATTERING (SANS)

The $\mathbf{Q}_1^{\mathrm{a}}$ reflection was also studied using the SANS setup on D33 (ILL) and SANS-I (PSI) beamlines. In accordance with our single crystal neutron diffraction results, no additional reflections were observed along the [010] direction, in the accessible momentum transfer range. At room temperature, the $|\mathbf{Q}|$-length for this reflection was found to be 0.1836(6) Å^{-1}, as shown in Fig.S7b. In real space it corresponds to a spiral pitch length of $\lambda_{\mathrm{s}} = 2\pi/|\mathbf{Q}| = 34.21(1)$ Å. Upon cooling $|\mathbf{Q}|$ changes to 0.2089(2) Å^{-1} prior to entering Phase I. The corresponding pitch length in real space decreases to 30.08(3) Å. This substantial change by 13.8% of the pitch length may be attributed to gradual change in anisotropic exchange interactions [50].

Magnetic field evolution of the $\mathbf{Q}_1^{\mathrm{a}}$ reflection was also studied by SANS in two complementary geometries compared to the one presented in the main text, (I) H || a || neutron beam (II) H || c^* $\perp$ neutron beam in Phase III. As described in the main text, Phase III is a helical spiral phase with moments rotating predominantly in the ab-plane. Therefore, applying magnetic field in any direction within the ab-plane should yield similar results. This has been confirmed by the results with magnetic field along the a-axis. As demonstrated in Fig. S7d, the intensity of the $\mathbf{Q}_1^{\mathrm{a}}$ reflection also exhibits a sudden decrease at H_{c1}, similar to $\mathbf{Q}_2^{\mathrm{a}}$ as presented in the main text (Fig. 3b), before completely vanishing at H_{c2}. Concomitantly, a sharp change is also observed in $|\mathbf{Q}|$ at H_{c1}, suggesting a spin reorientation process. The results of SND and SANS confirm that at H_{c1} the helical spiral flops into a cycloid in the bc-plane, with an additional ferromagnetic moment along the direction of the applied field (a-axis). The pitch length of the helical spiral transforms continuously until H_{c2}, with the most dramatic change from 31.4 Å to 22.4 Å observed in Phase IV. The almost 27.2% change has significant consequences in the intrinsic SSC and is significantly larger compared to the changes in the prototypical system governed by fluctuation-induced THE,

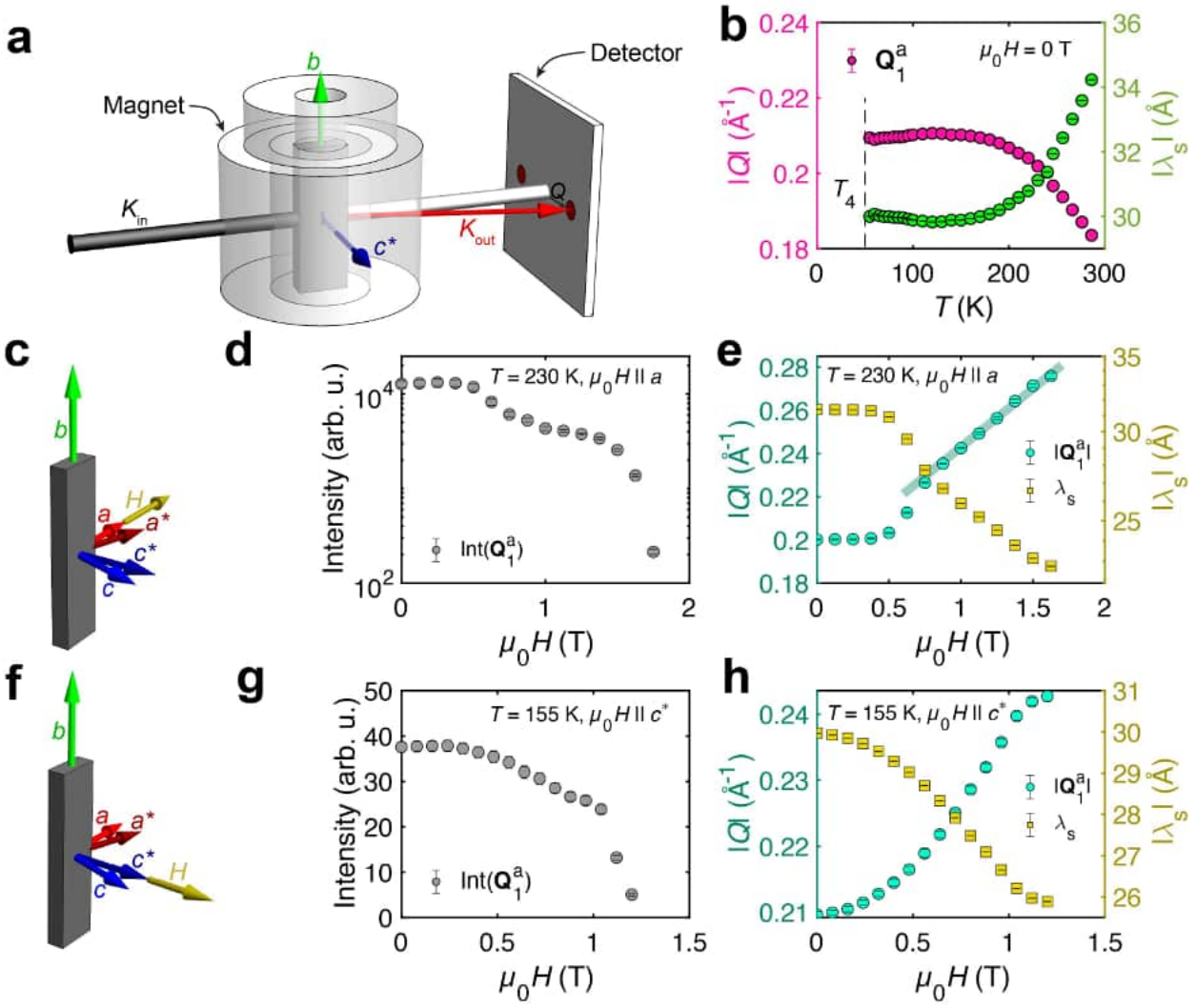

FIG. S7. **SANS studies on $\mathbf{Q}_1^a$ reflection of Fe_3Ga_4.** (a) Schematics of SANS experimental setup used for Fe_3Ga_4. (b) Temperature dependence of $\mathbf{Q}_1^a$ reflection as measured using small angle neutron scattering (SANS) measurements performed both on D33 (ILL) and SANS-I (PSI). The dashed vertical lines shown in both panels represent the boundary between Phase I and Phase III. Magnetic field evolution of (d) intensity and (e) $|\mathbf{Q}|$ of $\mathbf{Q}_1^a$ reflection measured in longitudinal geometry on SANS-I. Temperature of the sample was kept constant at 230 K, while magnetic field was varied along the a-axis. The straight line in panel-e represents a linear fit to the data in Phase IV. (g) (h) $\mathbf{Q}_1^a$ reflection was also measured in the transverse geometry on D33 (ILL). Temperature of the crystal was kept constant at 155 K, while magnetic field was applied parallel to $\mathbf{Q}$, approximately along c^*. (c),(f) represent the schematics of applied magnetic field with respect to the crystallographic axes.

YMn_6Sn_6.

In the second SANS geometry, magnetic field was applied perpendicular to the helix plane, along

the c^* direction. This configuration induces a conical state out of the helical spiral, as schematically shown in Figure 1e in the main text. A smooth change in intensity and $|\mathbf{Q}_1^a|$ (thus $|\lambda_s|$) is observed throughout the measured magnetic field range, before completely vanishing around 1.2 T. We presume this behaviour is due to a gradual transformation of the conical spiral towards the $\mathbf{k} = (0\ 0\ 1/2)$ antiferromagnetic state.

VI. ELECTRICAL TRANSPORT

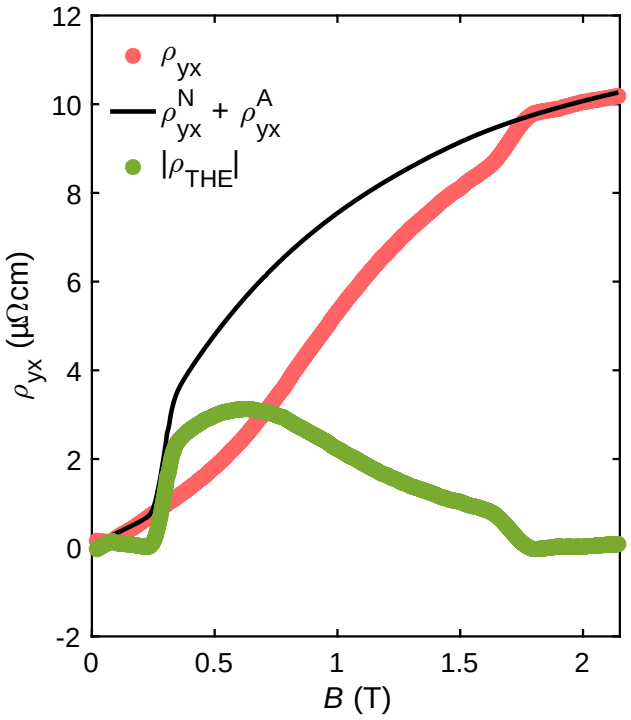

FIG. S8. **Extraction of ρ_{THE}.** The terms of the corrected measured ρ_{yx} (in red) are: sum of the normal (ρ_{yx}^{N}) and anomalous (ρ_{yx}^{A}) contributions (in black) and the topological ρ_{THE} term (in green).

Electrical Hall effect measurements were performed on a plate-type single crystal, as shown in main text Fig. 3. The Hall signal was first antisymmetrized with respect to external magnetic field, followed by an appropriate demagnetisation correction in order to account for the shape anisotropy of the crystal. The total Hall signal (ρ_{yx}) could be split in three terms: $\rho_{yx} = \rho_{yx}^{\mathrm{N}} + \rho_{yx}^{\mathrm{A}} + \rho_{\mathrm{THE}}$. We fitted the two first components, the normal and the anomalous contributions to: $\rho_{yx}^{\mathrm{N}} = \mu_0 R_0 H$ and $\rho_{yx}^{\mathrm{A}} = R_{\mathrm{A}} \rho_{xx}^2 M$, respectively. Here R_0 and $R_{\mathrm{A}}\rho_{xx}^2$ are the coefficients. The remaining topological Hall contribution ρ_{THE}, arises from the topological (or geometrical) nature of the real-space spin

structure. In YMn_6Sn_6 [19] ρ_{THE} had inverted U-shape and could be fitted as:

$$\rho_{\mathrm{THE}} = \kappa T H \cdot (1 - \frac{M^2}{M_s^2}), \text{ where } H \in [H_{\mathrm{c1}}\, H_{\mathrm{c2}}]. \quad (1)$$

As shown in Fig.S8, we observe significant ρ_{THE} in Phase IV of Fe_3Ga_4 , however, its shape is more complicated than in YMn_6Sn_6. We presume that this is due the complex phase diagram of Fe_3Ga_4 . At high temperatures (>300 K) ρ_{THE} deviates from the model of [19] due to vicinity of Phase V. Whereas, at low temperatures (200 K $< T <$ 300 K), it is significantly affected by the field-induced transition to Phase II.

Supplementary information for

"Fluctuation-driven topological Hall effect in room-temperature itinerant helimagnet Fe_3Ga_4"

Priya R. Baral,[1,2,3,*] Victor Ukleev,[1,4] Ivica Živković,[2] Youngro Lee,[2] Fabio Orlandi,[5] Pascal Manuel,[5] Yurii Skourski,[6] Lukas Keller,[1] Anne Stunault,[7] J. Alberto Rodríguez-Velamazán,[7] Robert Cubitt,[7] Arnaud Magrez,[2] Jonathan S. White,[1] Igor I. Mazin,[8,9] and Oksana Zaharko[1,†]

[1]*Laboratory for Neutron Scattering and Imaging (LNS), PSI Center for Neutron and Muon Sciences, 5232 Villigen PSI, Switzerland*

[2]*Institute of Physics, École Polytechnique Fédérale de Lausanne (EPFL), CH-1015 Lausanne, Switzerland*

[3]*Department of Applied Physics and Quantum-Phase Electronics Center, The University of Tokyo, Bunkyo-ku, Tokyo 113-8656, Japan*

[4]*Helmholtz-Zentrum Berlin für Materialien und Energie, D-14109 Berlin, Germany*

[5]*ISIS Facility, STFC Rutherford Appleton Laboratory, Harwell Science and Innovation Campus, Oxfordshire OX11 0QX, United Kingdom*

[6]*Dresden High Magnetic Field Laboratory (HLD-EMFL), Helmholtz-Zentrum Dresden-Rossendorf, 01328 Dresden, Germany*

[7]*Institut Laue–Langevin, 71 avenue des Martyrs, CS 20156, Grenoble, 38042 Cedex 9, France*

[8]*Department of Physics and Astronomy, George Mason University, Fairfax, VA 22030*

[9]*Center for Quantum Science and Engineering, George Mason University, Fairfax, VA 22030*

[*] baralp@g.ecc.u-tokyo.ac.jp

[†] oksana.zaharko@psi.ch

The supplementary materials contain additional information concerning single crystal X-ray diffraction, magnetisation, ac susceptibility, neutron diffraction, small angle neutron scattering as well as spherical neutron polarimetry data to support the results presented in the main text.

I. SINGLE CRYSTAL CHARACTERISATIONS

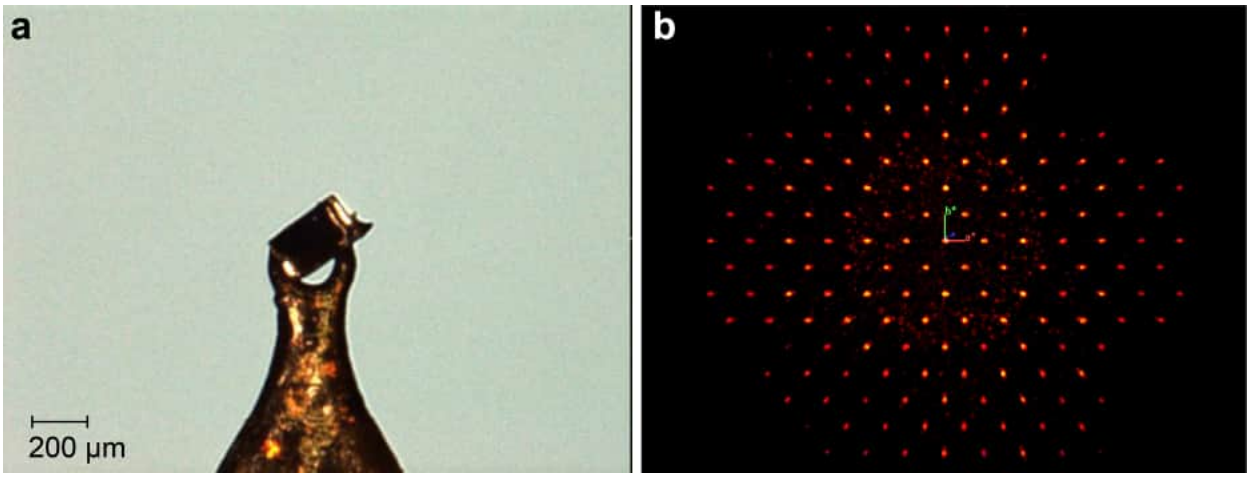

FIG. S1. **Single crystal X-ray diffraction. a**. A small Fe_3Ga_4 single crystal mounted on a holder for X-ray diffraction experiments. **b**. Reciprocal space map obtained at room temperature.

A preliminary quality check was performed on each single crystal sample used for this study via X-ray diffraction experiments both at room temperature as well as at 200 K. Here, we show results from one of our X-ray diffraction experiments. A small Fe_3Ga_4 crystal of size approximately 120 μm was mounted on a needle-type holder. We acquired a total of 2038 reflections to refine the crystal structure at 200 K. The best solution was found for the space group $C2/m$ (#12) with lattice constants as: 10.0966(5) Å, 7.6650(4) Å, 7.8655(4) Å, 90^0, $106.251(4)^0$, and 90^0. This unit cell matches quite well with the previous results [1].

II. BULK MAGNETOMETRY

Magnetisation and ac susceptibility measurements were also performed in Phase I and VI. A linear increase in $M(H)$, and thus a constant dM/dH is observed (in Fig. S2a) in both Phases until the first inflection point. Further we observe a slower increase in magnetisation until 14 T. High-field

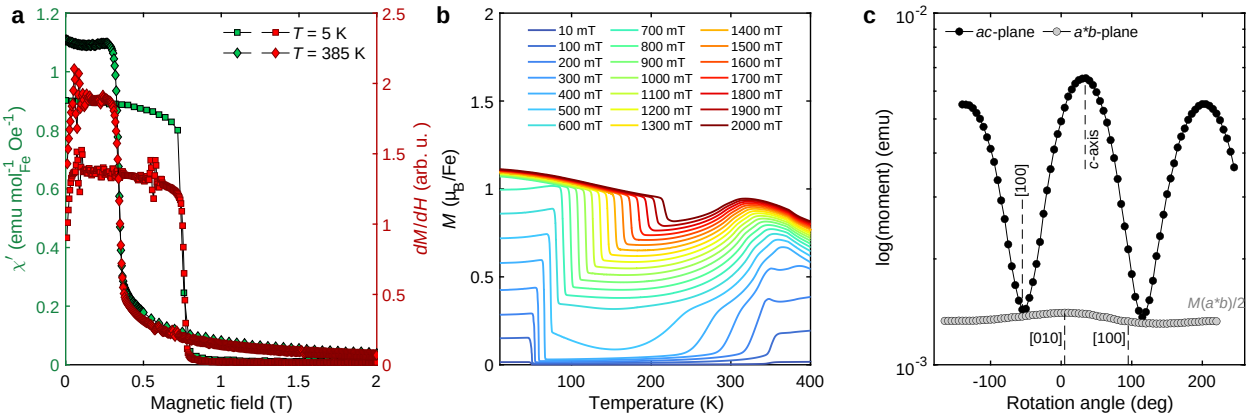

FIG. S2. **Additional magnetometry data on Fe_3Ga_4.**(a) Field evolution of isothermal dynamic ac-susceptibility χ' and static magnetisation M in Phases I and VI at temperatures 5 K and 385 K. (b) Temperature dependent magnetisation of a Fe_3Ga_4 single crystal with a series of constant magnetic fields applied along the b-axis. Each scan was measured between 5 K and 395 K in a sweep mode. (c) Angle dependent magnetisation data for a needle-type Fe_3Ga_4 single crystal measured at $T = 30$ K with 0.05 T constant magnetic field. Two distinct rotation planes, ac- and a^*b-, were selected similar to what is shown in Fig. **??**c.

magnetisation measured in Phase I at $T = 10$ K confirms that Fe_3Ga_4 does not attain saturation moment even until 30 T. The temperature scans shown in panel-b of Fig. S2, evidence for previously unreported Phase V and VII is quite clear. Multiple transitions are observed in $M(T)$ curves measured with lowest magnetic fields, for example 100 mT. While the drop observed with $\mu_0 H = 2$ T signifies the transition in and out of Phase IV from its adjacent phases. Magnetisation rotation measurements were also performed in Phase I, similar to the data shown in main text figure **??**c. As $m_c > m_a \geq m_b$ was also obtained in Phase I, we can conclude that magnetic anisotropy is similar for both Phases I and III.

III. SPHERICAL NEUTRON POLARIMETRY

Precise directional information about the magnetic order in Fe_3Ga_4 was obtained using the SNP experiment on the hot neutron source (D3) at the ILL. To interpret the data a local coordinate system for each reflection is chosen such that the x-axis is fixed along $\mathbf{Q}$ (shown in Fig. **??**a), the z-axis is vertical and y completes the right-handed Cartesian set. For each of the three incoming neutron polarisations P_x^{in}, P_y^{in} and P_z^{in} the three components in the scattered beam $P_{x,y,z}^{\text{out}}$ are analysed generating in total nine components of the resultant polarisation matrix. This matrix contains contributions of all domains scattering to the magnetic reflection and for each domain contains

polarisation vector P'' created during the scattering and polarisation tensor $\tilde{P}$. The polarisation tensor $\tilde{P}$ can be written as:

$$\tilde{P} = \begin{pmatrix} \frac{\mathbf{N}^2 - \mathbf{M}_\perp^2}{I_x} & -\frac{J_{nz}}{I_x} & \frac{J_{ny}}{I_x} \\ \frac{J_{nz}}{I_y} & \frac{\mathbf{N}^2 - \mathbf{M}_\perp^2 + R_{yy}}{I_y} & \frac{R_{yz}}{I_y} \\ -\frac{J_{ny}}{I_z} & \frac{R_{zy}}{I_z} & \frac{\mathbf{N}^2 - \mathbf{M}_\perp^2 + R_{zz}}{I_z} \end{pmatrix}$$

with P_i^{in} changing within the rows and P_j^{out} within the columns ($i, j = x, y, z$). Here $\mathbf{N}$ and $\mathbf{M}_\perp$ are the nuclear structure factor and the magnetic interaction vector, the projection of the magnetic structure factor orthogonal to $\mathbf{Q}$. The off-diagonal elements contain imaginary nuclear-magnetic interference terms J_{ni}=2 **Im**($\mathbf{N}(\mathbf{Q})\mathbf{M}^*_{\perp i}(\mathbf{Q})$), real R_{ij}=2 **Re**($\mathbf{M}_{\perp i}(\mathbf{Q})\mathbf{M}^*_{\perp j}(\mathbf{Q})$), and intensity terms $I_{i=x,y,z}$ are $I_x = \mathbf{N}^2 + \mathbf{M}_\perp^2 + P_x J_{yz}$, $I_{y/z} = \mathbf{N}^2 + \mathbf{M}_\perp^2 + P_{y/z} R_{n(y/z)}$. The polarisation vector P''

$$P'' = \begin{pmatrix} \frac{J_{nz}}{I} \\ \frac{R_{ny}}{I} \\ \frac{R_{nz}}{I} \end{pmatrix}.$$

contains, the so-called magnetic interference terms $J_{ij} = 2\mathbf{Im}(\mathbf{M}_{\perp i}(\mathbf{Q})\mathbf{M}^*_{\perp j}(\mathbf{Q}))$, and the real nuclear-magnetic interference terms $R_{ni} = 2\mathbf{Re}(\mathbf{N}(\mathbf{Q})\mathbf{M}^*_{\perp i}(\mathbf{Q}))$.

To index magnetic reflections identified in our SNP experiments precisely, we compared them with higher resolution results from WISH, ZEBRA and DMC. Below the polarisation matrices for various reflections at different temperatures are listed.

Phase I: T = 10 K

k = 0 reflections

We could differentiate two families of reflections. The family **Q** = (4,0,1), (2,0,3), (2,0,-4), (0,0,4), (-2,0,4), and (-4,0,-1) has $P_{xx} = P_{yy} = P_{zz} = 1$ thus, the reflections are purely nuclear. For the family **Q** = (2,0,1), (2,0,0), (-2,0,3), (-2,0,2), (-4,0,3) and (4,0,-1) the P_{xx} and P_{zz} elements are reduced. This could be due to depolarisation of neutrons by combined effect of the global ferromagnetic contribution along c and of the local ferromagnetic components within the slabs along a. This combined field is along the y-local coordinate axes of this second family of reflections, *i. e.* approximately along (101). The resultant polarisation matrices are:

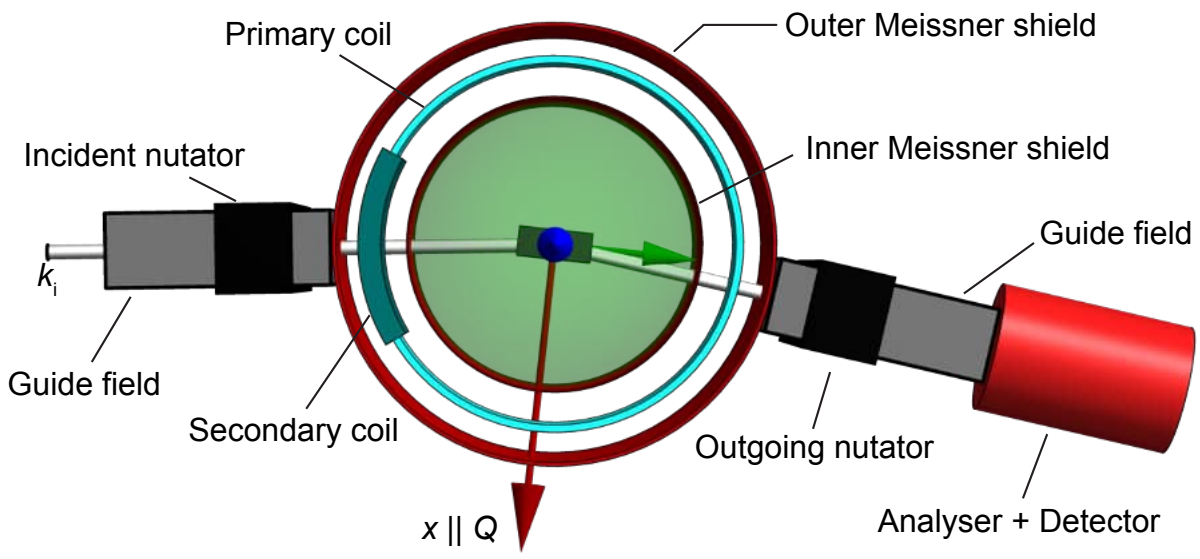

FIG. S3. **Spherical neutron polarimetry experiment using the CRYOPAD setup on D3 (ILL).** Schematics of the CRYOPAD setup used for our SNP experiment on the D3 (ILL) beamline. The single crystal is centered inside two concentric Meissner shields achieving a net zero magnetic field condition. The x-coordinate of the local polarisation axis is chosen such that it coincides with the direction of **Q**. The remaining local axes (y and z) are chosen in order to satisfy the right hand coordinate system. Using the guide field, the incoming polarisation of the neutron beam is tuned to match one of the local axes of a particular Bragg reflection, while all three components of the outgoing polarisation vector is measured.

1. **Q** = (4.0, 0.0, 1.0)

$$\begin{pmatrix} 1.05 \pm 0.14 & 0.04 \pm 0.01 & -0.03 \pm 0.01 \\ -0.06 \pm 0.01 & 1.06 \pm 0.14 & -0.03 \pm 0.01 \\ -0.01 \pm 0.01 & 0.02 \pm 0.01 & 1.01 \pm 0.01 \end{pmatrix}$$

2. **Q** = (2.0, 0.0, 3.0)

$$\begin{pmatrix} 0.99 \pm 0.04 & 0.07 \pm 0.06 & -0.02 \pm 0.06 \\ -0.08 \pm 0.06 & 1.05 \pm 0.03 & 0.06 \pm 0.06 \\ 0.04 \pm 0.05 & 0.02 \pm 0.08 & 0.99 \pm 0.03 \end{pmatrix}$$

3. **Q** = (2.0, 0.0, 1.0)

$$\begin{pmatrix} 0.78 \pm 0.03 & 0.02 \pm 0.04 & -0.03 \pm 0.04 \\ -0.05 \pm 0.04 & 1.01 \pm 0.03 & 0.04 \pm 0.04 \\ 0.05 \pm 0.04 & -0.03 \pm 0.04 & 0.79 \pm 0.03 \end{pmatrix}$$

4. **Q** = (2.0, 0.0, 0.0)

$$\begin{pmatrix} 0.61 \pm 0.05 & 0.05 \pm 0.05 & -0.04 \pm 0.05 \\ 0.01 \pm 0.05 & 1.12 \pm 0.04 & 0.04 \pm 0.05 \\ 0.01 \pm 0.06 & 0.01 \pm 0.05 & 0.62 \pm 0.04 \end{pmatrix}$$

5. **Q** = (2.0, 0.0, -4.0)

$$\begin{pmatrix} 0.99 \pm 0.03 & -0.02 \pm 0.04 & -0.01 \pm 0.04 \\ -0.02 \pm 0.04 & 1.04 \pm 0.02 & 0.05 \pm 0.04 \\ -0.03 \pm 0.04 & 0.03 \pm 0.04 & 0.99 \pm 0.03 \end{pmatrix}$$

6. **Q** = (0.0, 0.0, 4.0)

$$\begin{pmatrix} 0.99 \pm 0.02 & 0.04 \pm 0.03 & -0.05 \pm 0.03 \\ -0.07 \pm 0.04 & 0.99 \pm 0.02 & 0.06 \pm 0.03 \\ -0.03 \pm 0.04 & 0.07 \pm 0.04 & 0.99 \pm 0.02 \end{pmatrix}$$

7. **Q** = (-2.0, 0.0, 4.0)

$$\begin{pmatrix} 0.99 \pm 0.02 & -0.01 \pm 0.03 & 0.01 \pm 0.03 \\ -0.05 \pm 0.03 & 1.01 \pm 0.02 & -0.05 \pm 0.03 \\ -0.01 \pm 0.03 & 0.05 \pm 0.03 & 1.00 \pm 0.02 \end{pmatrix}$$

8. **Q** = (-2.0, 0.0, 3.0)

$$\begin{pmatrix} 0.85 \pm 0.03 & 0.03 \pm 0.04 & -0.01 \pm 0.04 \\ -0.07 \pm 0.04 & 1.02 \pm 0.03 & -0.04 \pm 0.04 \\ 0.05 \pm 0.04 & -0.05 \pm 0.04 & 0.87 \pm 0.03 \end{pmatrix}$$

9. **Q** = (-2.0, 0.0, 2.0)

$$\begin{pmatrix} 0.38 \pm 0.02 & 0.04 \pm 0.02 & -0.03 \pm 0.02 \\ 0.04 \pm 0.02 & 1.05 \pm 0.02 & -0.05 \pm 0.02 \\ -0.02 \pm 0.02 & 0.01 \pm 0.02 & 0.38 \pm 0.02 \end{pmatrix}$$

10. **Q** = (-4.0, 0.0, 3.0)

$$\begin{pmatrix} 0.80 \pm 0.04 & 0.09 \pm 0.02 & -0.04 \pm 0.03 \\ -0.01 \pm 0.03 & 1.02 \pm 0.06 & -0.02 \pm 0.03 \\ -0.03 \pm 0.03 & -0.01 \pm 0.03 & 0.78 \pm 0.02 \end{pmatrix}$$

11. **Q** = (-4.0, 0.0, -1.0)

$$\begin{pmatrix} 1.02 \pm 0.01 & 0.01 \pm 0.02 & -0.01 \pm 0.02 \\ -0.08 \pm 0.02 & 0.99 \pm 0.01 & 0.01 \pm 0.01 \\ 0.00 \pm 0.01 & 0.05 \pm 0.01 & 1.01 \pm 0.01 \end{pmatrix}$$

12. **Q** = (4.0, 0.0, -1.0)

$$\begin{pmatrix} 0.42 \pm 0.04 & -0.01 \pm 0.04 & -0.02 \pm 0.04 \\ -0.16 \pm 0.04 & 0.94 \pm 0.03 & -0.01 \pm 0.04 \\ -0.03 \pm 0.04 & 0.09 \pm 0.04 & 0.47 \pm 0.04 \end{pmatrix}$$

k = (0 0 1/2) reflections

1. **Q** = (0.0, 0.0, -1/2)

$$\begin{pmatrix} -0.99 \pm 0.03 & -0.03 \pm 0.03 & 0.05 \pm 0.03 \\ 0.01 \pm 0.03 & 0.99 \pm 0.02 & 0.07 \pm 0.02 \\ 0.02 \pm 0.02 & 0.07 \pm 0.03 & -1.00 \pm 0.03 \end{pmatrix}$$

2. **Q** = (0.0, 0.0, 1/2)

$$\begin{pmatrix} -1.02 \pm 0.03 & -0.01 \pm 0.03 & -0.01 \pm 0.03 \\ 0.03 \pm 0.02 & 1.01 \pm 0.03 & -0.10 \pm 0.02 \\ 0.02 \pm 0.04 & -0.09 \pm 0.03 & -1.01 \pm 0.03 \end{pmatrix}$$

Phase III: T = 155 K

k = 0 reflections

1. **Q**= (4.0, 0.0, 1.0)

$$\begin{pmatrix} 1.02 \pm 0.01 & 0.02 \pm 0.02 & -0.03 \pm 0.02 \\ -0.09 \pm 0.02 & 0.99 \pm 0.01 & -0.01 \pm 0.02 \\ -0.02 \pm 0.02 & 0.07 \pm 0.02 & 1.00 \pm 0.01 \end{pmatrix}$$

2. **Q** = (2.0, 0.0, 1.0)

$$\begin{pmatrix} 1.07 \pm 0.05 & 0.04 \pm 0.06 & 0.11 \pm 0.07 \\ -0.11 \pm 0.06 & 0.93 \pm 0.05 & -0.05 \pm 0.06 \\ -0.12 \pm 0.06 & 0.07 \pm 0.07 & 0.96 \pm 0.06 \end{pmatrix}$$

3. **Q** = (2.0, 0.0, 0.0)

$$\begin{pmatrix} 0.90 \pm 0.05 & -0.06 \pm 0.05 & -0.03 \pm 0.05 \\ -0.02 \pm 0.06 & 0.97 \pm 0.05 & 0.05 \pm 0.07 \\ -0.01 \pm 0.12 & -0.14 \pm 0.06 & 1.05 \pm 0.05 \end{pmatrix}$$

4. **Q** = (-2.0, 0.0, 4.0)

$$\begin{pmatrix} 0.97 \pm 0.02 & -0.01 \pm 0.03 & -0.04 \pm 0.04 \\ -0.04 \pm 0.03 & 0.98 \pm 0.02 & 0.01 \pm 0.03 \\ -0.04 \pm 0.04 & 0.02 \pm 0.04 & 0.97 \pm 0.02 \end{pmatrix}$$

k = $(\alpha\ 0\ \gamma)$ reflections

5. $\mathbf{Q}_2^{\mathrm{a}}$ = (0.007, 0.00, 0.759)

$$\begin{pmatrix} -1.04 \pm 0.03 & -0.04 \pm 0.06 & -0.01 \pm 0.07 \\ -0.43 \pm 0.05 & 0.01 \pm 0.04 & -0.01 \pm 0.05 \\ -0.48 \pm 0.05 & -0.02 \pm 0.04 & -0.06 \pm 0.05 \end{pmatrix}$$

6. $\mathbf{Q}_1^{\mathrm{b}}$ = (1.99, 0.00, 1.28)

$$\begin{pmatrix} -1.01 \pm 0.22 & -0.01 \pm 0.13 & 0.15 \pm 0.35 \\ 0.37 \pm 0.08 & -0.53 \pm 0.09 & -0.13 \pm 0.17 \\ 0.29 \pm 0.12 & 0.17 \pm 0.21 & 0.34 \pm 0.12 \end{pmatrix}$$

7. -$\mathbf{Q}_2^{\mathrm{a}}$ = (-0.01, 0.00, -0.73)

$$\begin{pmatrix} -1.05 \pm 0.04 & -0.02 \pm 0.04 & -- \\ -0.28 \pm 0.05 & -0.01 \pm 0.06 & -- \\ -0.31 \pm 0.05 & -- & 0.02 \pm 0.05 \end{pmatrix}$$

Phase III: T = 288 K

k = 0 reflections

1. **Q** = (2.0, 0.0, 0.0)

$$\begin{pmatrix} 1.04 \pm 0.17 & 0.03 \pm 0.18 & -0.07 \pm 0.16 \\ -0.32 \pm 0.15 & 0.95 \pm 0.16 & -0.22 \pm 0.16 \\ -0.15 \pm 0.18 & 0.18 \pm 0.19 & 0.94 \pm 0.16 \end{pmatrix}$$

2. $\mathbf{Q}$ = (4.0, 0.0, 1.0)

$$\begin{pmatrix} 1.00 \pm 0.01 & 0.04 \pm 0.01 & -0.01 \pm 0.01 \\ -0.05 \pm 0.01 & 1.01 \pm 0.01 & 0.02 \pm 0.01 \\ -0.01 \pm 0.01 & 0.03 \pm 0.01 & 0.99 \pm 0.01 \end{pmatrix}$$

$\mathbf{k} = (\alpha\ 0\ \gamma)$ reflections

1. -$\mathbf{Q}_1^a$ = (-0.01, 0.00, -0.73)

$$\begin{pmatrix} -1.05 \pm 0.06 & -0.01 \pm 0.06 & -0.07 \pm 0.07 \\ -0.63 \pm 0.07 & 0.02 \pm 0.08 & 0.01 \pm 0.11 \\ -0.81 \pm 0.09 & 0.09 \pm 0.09 & -0.15 \pm 0.09 \end{pmatrix}.$$

Here, red and blue represent the extreme values of general matrix elements, P_{xy}, that is +1 and -1, respectively. While the numbers shown in green are intermediate.

IV. SINGLE CRYSTAL NEUTRON DIFFRACTION (SND) AT BASE TEMPERATURE

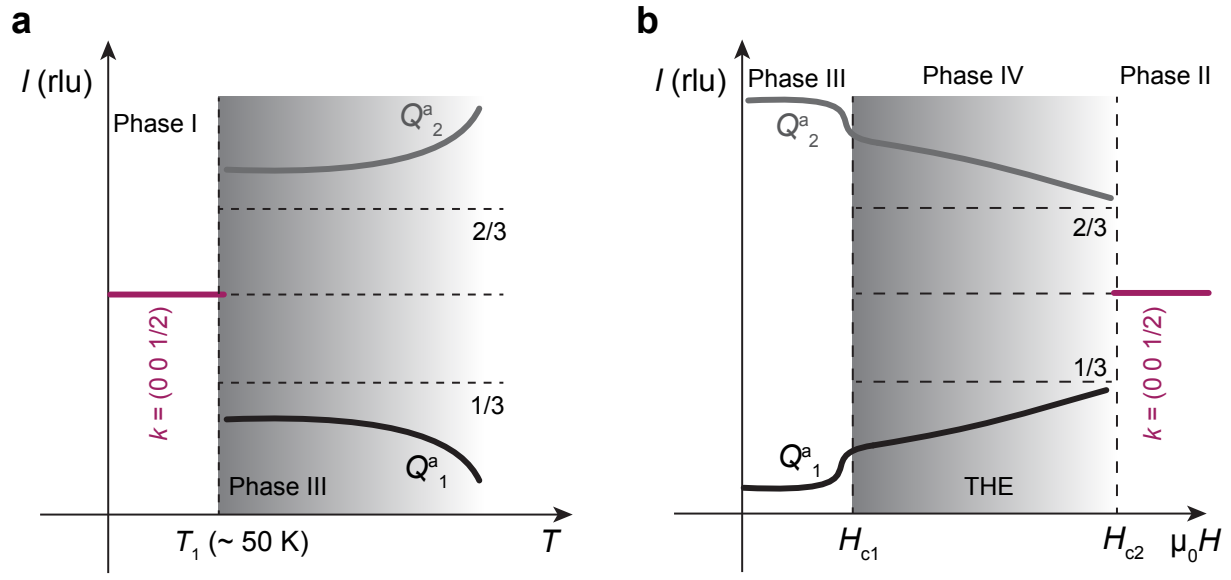

FIG. S4. **Temperature and field dependence of magnetic reflections in Fe_3Ga_4.** Behaviour of ICM reflections together with $\mathbf{Q} = (0, 0, 1/2)$ reflection was reconstructed using results from all the neutron scattering measurements described in the text. Panel-**a** shows the schematics of temperature dependece while magnetic field dependence is shown in Panel-**b**.

The temperature and magnetic field dependencies of the commensurate and incommensurate magnetic reflections obtained by neutron scattering experiments are schematically shown in Fig. S4. The crucial finding from neutron diffraction is the appearance of new magnetic reflections below T_1, which can be indexed with the propagation vector $\mathbf{k}$ = (0 0 1/2). The commensurate antiferromagnetic state was not detected in previous studies [2]. Figure S6a shows a part of the reciprocal space of Fe_3Ga_4 obtained in Phase I with the WISH diffractometer. The $\mathbf{Q}$ = (0,0,$\pm$1/2) reflections are very strong, signaling that magnetic moments lie within the ab-plane. Further, the polarisation matrix measured for the $\mathbf{Q}$ = (0,0,$\pm$1/2) reflection on the D3 diffractometer at ILL unambiguously implies that the magnetic moments point along the a-crystal axis: the initial polarisation along the local z-axis (b-crystal axis) flips, while polarisation measured along the y-axis is not changed. A zero field 10 K dataset containing 84 $\mathbf{k} = (0\ 0\ 1/2)$ reflections was collected on the ZEBRA diffractometer. Most of the magnetic reflections were weak and several models from the twelve maximal magnetic space groups proposed by BCS software [3] had similar goodness of fit. We developed the model reconciling results of SND, SNP, and magnetometry. Magnetic moments are constrained to two independent parameters 1.10(6)μ_B/Fe for Fe1, Fe2, Fe3 and 1.47(8)μ_B/Fe for Fe4 in the MSG C2'/c (15.87). The model, in Fig.S6c, comprises ferromagnetic slabs with moments pointing along the a-axis, while neighbouring slabs are aligned opposite to each other.

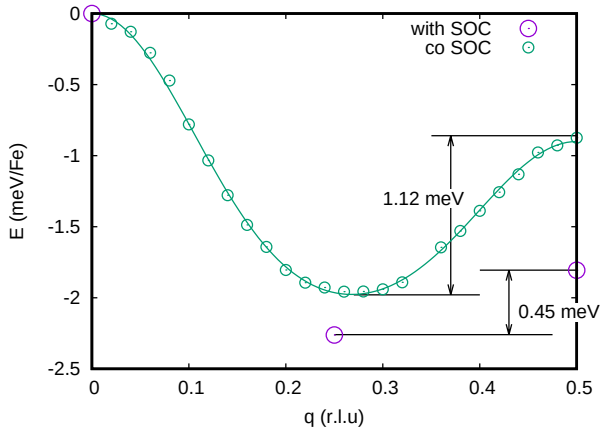

FIG. S5. **Energy landscape of magnetic states.** Energy of various spin states, with and without spin orbit coupling, as a function of q_z obtained from density functional theory calculations.

We observe a narrow coexisting region between Phase I and Phase III around T_1, as shown in Fig. **??**a. Below T_1 in zero field, a spontaneous magnetisation develops in Fe_3Ga_4. In our bulk measurements this is witnessed by a rise of magnetisation at T_1 and a hysteresis in the isothermal magnetisation loop. The moment value at 5 K and 10 mT is only 0.15 μ_B/Fe, it steeply increases

till 0.75 T, where is reaches 0.95 $\mu_{\rm B}$/Fe, and keeps rising at higher fields with moderate increment. Similar moment values are obtained from magnetisation data published by Mendez *et al.* [4] and Wilfong *et al.* [5]. In the single crystal neutron diffraction study of Wu *et al.* [2] the net $\mathbf{k}$=0 moment is assumed to point along the c-axis and the refined value is 1.4(2) μ_B/Fe. We observe the increased intensity of $\mathbf{Q}$ = (2,0,1), similar to Wu *et. al.* [2]. In Phase I, we detect an intriguing reduction of the elements P_{xx} and P_{zz} of the polarization matrices for the reflections $\mathbf{k}$ = 0 located in the zone orthogonal to the [101] direction (Fig. **??**b). This reduction most probably arises from depolarisation of the x and z-components by the ferromagnetic contribution, which is along [101], not along c.

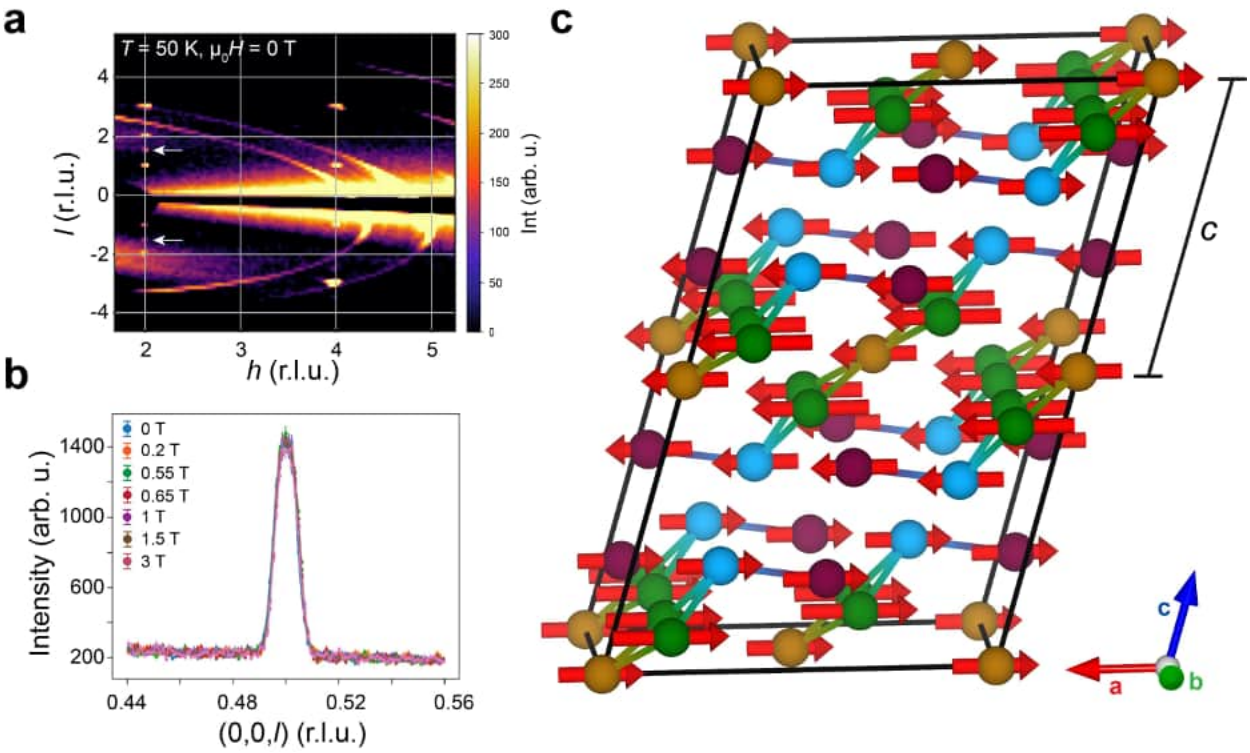

FIG. S6. **Single crystal neutron diffraction in Phase I.** (a) Reciprocal space map for Fe_3Ga_4 obtained in Phase I at 50 K. The white arrows indicate some of the weak (0,0,l) reflections in the ($h0l$) scattering plane. (b) The intensity of the $\mathbf{Q} = (0, 0, 0.5)$ peak was measured with the WISH diffractometer at 50 K, and no noticeable difference was observed up to 3 T magnetic field. (c) Magnetic structure of Fe_3Ga_4 as determined at T = 10 K from single crystal neutron diffraction experiments. Ga-atoms have been removed for clarity. The magnetic unit cell with doubled c comprises two Fe-slabs with magnetic moments along or opposite to the a-axis.

We further identify that the propagation vector $\mathbf{k}$=(0 0 1/2) persists in Phase II. In our diffraction experiment in magnetic field on WISH the intensity of the (0,0,1/2) reflection does not change

in fields from 0 T till 3 T (see Fig. S6b). We presume that $\mathbf{k}$=0 and $\mathbf{k}$=(0 0 1/2) contributions could be combined into an overall ferrimagnetic structure. The magnetisation discontinuity at H_{c1} (0.7 T at 5 K, shown in Fig. S2a) suggests that at H_{c1} the field selection of domains with the favourable ferromagnetic component takes place. The inset of Fig. **??**b shows that no further metamagnetic transitions occur till 30 T and magnetisation keeps steadily rising. Thus the canted ferrimagnetic structure with collinear AFM component along a and growing net component along b extends to very high fields, opposite to the presumptions of previous studies. To reach the fully polarised ferromagnetic state fields above 30 T are necessary.

V. SMALL ANGLE NEUTRON SCATTERING (SANS)

The $\mathbf{Q}_1^{\mathrm{a}}$ reflection was also studied using the SANS setup on D33 (ILL) and SANS-I (PSI) beamlines. In accordance with our single crystal neutron diffraction results, no additional reflections were observed along the [010] direction, in the accessible momentum transfer range. At room temperature, the $|\mathbf{Q}|$-length for this reflection was found to be 0.1836(6) Å^{-1}, as shown in Fig.S7b. In real space it corresponds to a spiral pitch length of $\lambda_{\mathrm{s}} = 2\pi/|\mathbf{Q}| = 34.21(1)$ Å. Upon cooling $|\mathbf{Q}|$ changes to 0.2089(2) Å^{-1} prior to entering Phase I. The corresponding pitch length in real space decreases to 30.08(3) Å. This substantial change by 13.8% of the pitch length may be attributed to gradual change in anisotropic exchange interactions [6].

Magnetic field evolution of the $\mathbf{Q}_1^{\mathrm{a}}$ reflection was also studied by SANS in two complementary geometries compared to the one presented in the main text, (I) H || a || neutron beam (II) H || c^* $\perp$ neutron beam in Phase III. As described in the main text, Phase III is a helical spiral phase with moments rotating predominantly in the ab-plane. Therefore, applying magnetic field in any direction within the ab-plane should yield similar results. This has been confirmed by the results with magnetic field along the a-axis. As demonstrated in Fig. S7d, the intensity of the $\mathbf{Q}_1^{\mathrm{a}}$ reflection also exhibits a sudden decrease at H_{c1}, similar to $\mathbf{Q}_2^{\mathrm{a}}$ as presented in the main text (Fig. **??**b), before completely vanishing at H_{c2}. Concomitantly, a sharp change is also observed in $|\mathbf{Q}|$ at H_{c1}, suggesting a spin reorientation process. The results of SND and SANS confirm that at H_{c1} the helical spiral flops into a cycloid in the bc-plane, with an additional ferromagnetic moment along the direction of the applied field (a-axis). The pitch length of the helical spiral transforms continuously until H_{c2}, with the most dramatic change from 31.4 Å to 22.4 Å observed in Phase IV. The almost 27.2% change has significant consequences in the intrinsic SSC and is significantly larger compared to the changes in the prototypical system governed by fluctuation-induced THE,

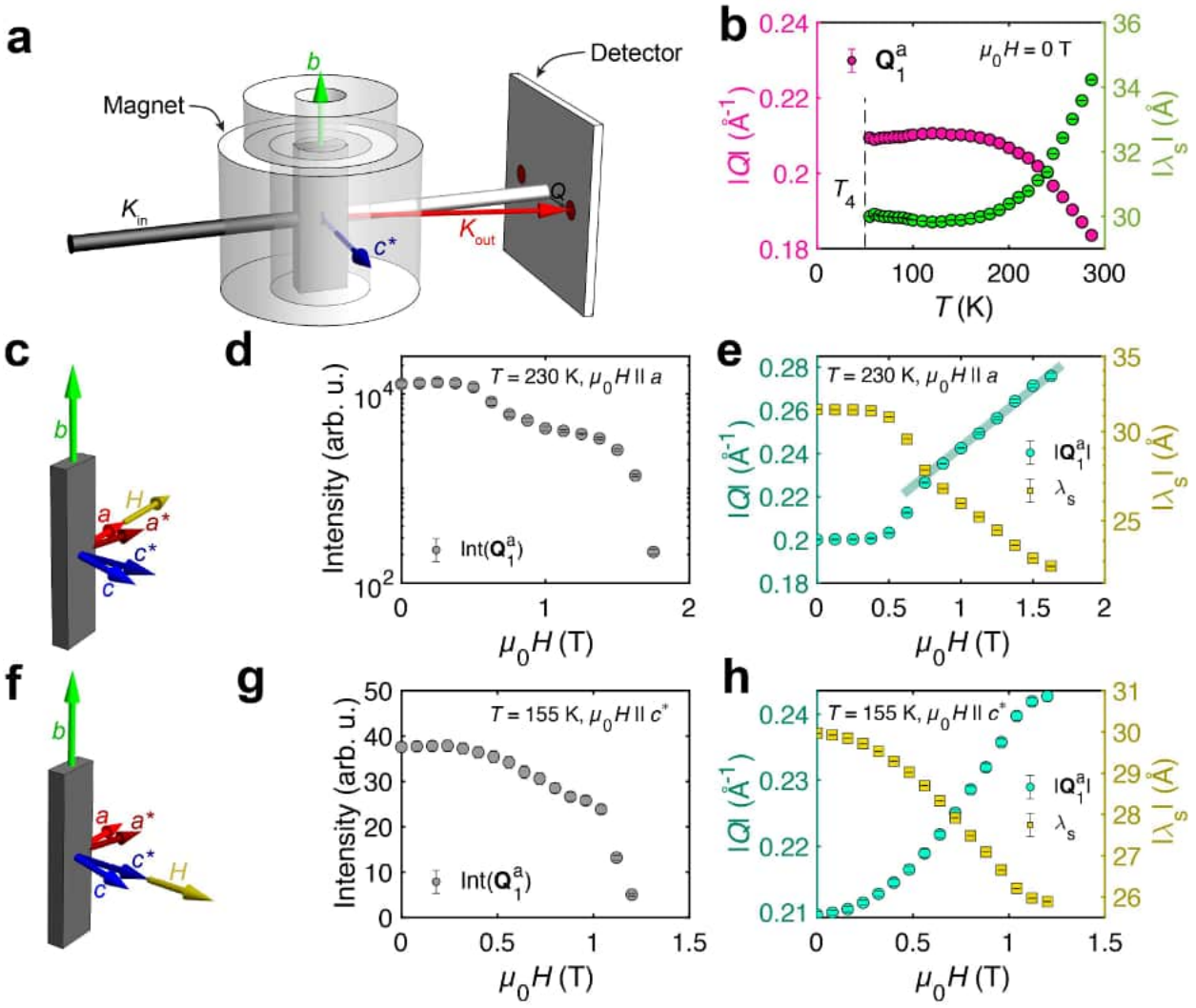

FIG. S7. **SANS studies on $\mathbf{Q}_1^a$ reflection of Fe_3Ga_4.** (a) Schematics of SANS experimental setup used for Fe_3Ga_4. (b) Temperature dependence of $\mathbf{Q}_1^a$ reflection as measured using small angle neutron scattering (SANS) measurements performed both on D33 (ILL) and SANS-I (PSI). The dashed vertical lines shown in both panels represent the boundary between Phase I and Phase III. Magnetic field evolution of (d) intensity and (e) $|\mathbf{Q}|$ of $\mathbf{Q}_1^a$ reflection measured in longitudinal geometry on SANS-I. Temperature of the sample was kept constant at 230 K, while magnetic field was varied along the a-axis. The straight line in panel-e represents a linear fit to the data in Phase IV. (g) (h) $\mathbf{Q}_1^a$ reflection was also measured in the transverse geometry on D33 (ILL). Temperature of the crystal was kept constant at 155 K, while magnetic field was applied parallel to $\mathbf{Q}$, approximately along c^*. (c),(f) represent the schematics of applied magnetic field with respect to the crystallographic axes.

YMn_6Sn_6.

In the second SANS geometry, magnetic field was applied perpendicular to the helix plane, along

the c^* direction. This configuration induces a conical state out of the helical spiral, as schematically shown in Figure **??**e in the main text. A smooth change in intensity and $|\mathbf{Q}_1^{\mathrm{a}}|$ (thus $|\lambda_{\mathrm{s}}|$) is observed throughout the measured magnetic field range, before completely vanishing around 1.2 T. We presume this behaviour is due to a gradual transformation of the conical spiral towards the $\mathbf{k}$ = (0 0 1/2) antiferromagnetic state.

VI. ELECTRICAL TRANSPORT

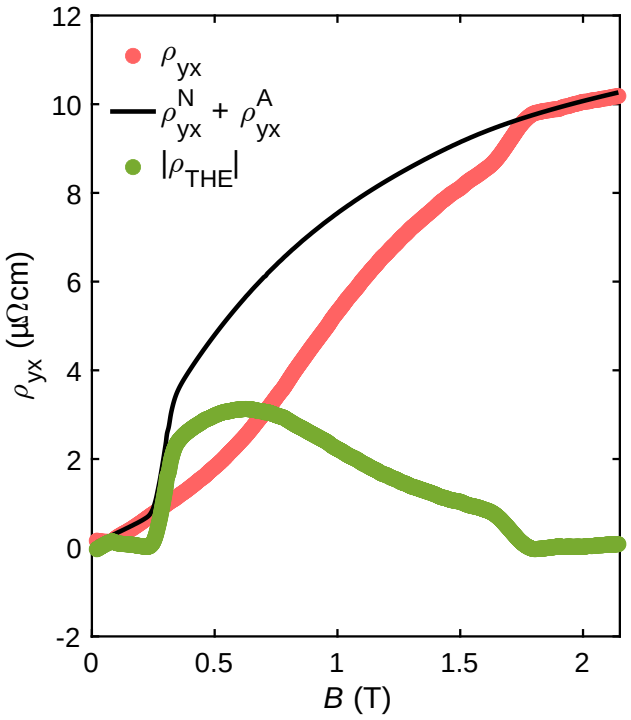

FIG. S8. **Extraction of ρ_{THE}.** The terms of the corrected measured ρ_{yx} (in red) are: sum of the normal (ρ^{N}_{yx}) and anomalous (ρ^{A}_{yx}) contributions (in black) and the topological ρ_{THE} term (in green).

Electrical Hall effect measurements were performed on a plate-type single crystal, as shown in main text Fig. **??**. The Hall signal was first antisymmetrized with respect to external magnetic field, followed by an appropriate demagnetisation correction in order to account for the shape anisotropy of the crystal. The total Hall signal (ρ_{yx}) could be split in three terms: $\rho_{yx} = \rho^{\mathrm{N}}_{yx} + \rho^{\mathrm{A}}_{yx} + \rho_{\mathrm{THE}}$. We fitted the two first components, the normal and the anomalous contributions to: $\rho^{\mathrm{N}}_{yx} = \mu_0 R_0 H$ and $\rho^{\mathrm{A}}_{yx} = R_{\mathrm{A}} \rho^2_{xx} M$, respectively. Here R_0 and $R_{\mathrm{A}}\rho^2_{xx}$ are the coefficients. The remaining topological Hall contribution ρ_{THE}, arises from the topological (or geometrical) nature

of the real-space spin structure. In YMn_6Sn_6 [7] ρ_{THE} had inverted U-shape and could be fitted as:

$$\rho_{\mathrm{THE}} = \kappa T H \cdot (1 - \frac{M^2}{M_s^2}), \text{ where } H \in [H_{\mathrm{c1}}\, H_{\mathrm{c2}}]. \quad (1)$$

As shown in Fig.S8, we observe significant ρ_{THE} in Phase IV of Fe_3Ga_4 , however, its shape is more complicated than in YMn_6Sn_6. We presume that this is due the complex phase diagram of Fe_3Ga_4 . At high temperatures (>300 K) ρ_{THE} deviates from the model of [7] due to vicinity of Phase V. Whereas, at low temperatures (200 K $< T <$ 300 K), it is significantly affected by the field-induced transition to Phase II.

---

[1] M. Philippe, B. Malaman, B. Roques, A. Courtois, and J. Protas, Structures cristallines des phases Fe_3Ga_4 et Cr_3Ga_4, Acta Crystallographica Section B: Structural Crystallography and Crystal Chemistry **31**, 477 (1975).

[2] Y. Wu, Z. Ning, H. Cao, G. Cao, K. A. Benavides, S. Karna, G. T. McCandless, R. Jin, J. Y. Chan, W. Shelton, *et al.*, Spin density wave instability in a ferromagnet, Scientific Reports **8**, 5225 (2018).

[3] J. Perez-Mato, S. Gallego, E. Tasci, L. Elcoro, G. de la Flor, and M. Aroyo, Symmetry-based computational tools for magnetic crystallography, Annual Review of Materials Research **45**, 217 (2015).

[4] J. H. Mendez, C. E. Ekuma, Y. Wu, B. W. Fulfer, J. C. Prestigiacomo, W. A. Shelton, M. Jarrell, J. Moreno, D. P. Young, P. W. Adams, A. Karki, R. Jin, J. Y. Chan, and J. F. DiTusa, Competing magnetic states, disorder, and the magnetic character of Fe_3Ga_4, Phys. Rev. B **91**, 144409 (2015).

[5] B. Wilfong, A. Fedorko, D. R. Baigutlin, O. N. Miroshkina, X. Zhou, G. M. Stephen, A. L. Friedman, V. Sharma, O. Bishop, R. Barua, *et al.*, Helical spin ordering in room-temperature metallic antiferromagnet Fe_3Ga_4, Journal of Alloys and Compounds **917**, 165532 (2022).

[6] P. R. Baral, O. I. Utesov, C. Luo, F. Radu, A. Magrez, J. S. White, and V. Ukleev, Direct observation of exchange anisotropy in the helimagnetic insulator Cu_2OSeO_3, Phys. Rev. Res. **5**, L032019 (2023).

[7] N. J. Ghimire, R. L. Dally, L. Poudel, D. C. Jones, D. Michel, N. T. Magar, M. Bleuel, M. A. McGuire, J. S. Jiang, J. F. Mitchell, J. W. Lynn, and I. I. Mazin, Competing magnetic phases and fluctuation-driven scalar spin chirality in the kagome metal YMn_6Sn_6, Science Advances **6**, eabe2680 (2020).